Table of contents

List of tables

Figure list

Acknowledgement

This thesis is a result of a three years study in the Laboratory of Biomaterials and Bioengineering of the department of mining, metallurgical and materials engineering and the University-Hospital Research Center of Laval University. This study would not have been accomplished without all the support that I have received. Therefore, I would like to make use of this portion of my thesis to acknowledge all of those who have supported me.

First of all, I would like to thank my director, professor Diego Mantovani, who gave me the opportunity to start doing this research at Laval University and supported me throughout these last years. His advice paved the way to achieve this MSc degree.

I would also like to thank all the advices, supports, and encouragement that I have received from professor Gaétan Laroche, my co-supervisor, who has always made himself available for discussion. I admire his great personality and I am proud of working under his supervision.

I have spent nearly the entire four years in direct contact with the research professionals of our group: Dr. Stéphane Turgeon and Dr. Pascale Chevallier. Beside their availability and scientific and technical support that deserve a lot of appreciation, I would also like to express my warmest gratitude for the welcoming environment that they established from the very first day. This kind gesture made it easy to surpass any kind of difficulty for the last three years.

Next, I would like to acknowledge my appreciation to Dr. Ranna Tolouei for her generous support and Maxime Cloutier for his scientific and technical help. I would also like to thank the rest of the members of the group. I am proud of having such good friends.

Finally, I must express my profound gratitude to my family, especially my wife Parnaz and my parents for their unfailing support and encouragement throughout the years of this study. I would also like to acknowledge my appreciation for the continuous support and encouragement that my brothers Farshad and Farzad have given me. This accomplishment would not have been possible without them.

Farid Anooshehpour

April 2016

1 Introduction

Carbon is a nonmetallic element with four valence electrons available to form different covalent chemical bonds. It lets various configurations of carbon atoms in different structures to exist (known as carbon allotropes). Graphite and diamond are among the natural form of carbon. However, there are other more recently discovered forms of carbon such as: graphene, fullerene, carbon nanotube, amorphous carbon. Each has its own properties and its own specific application.

Diamond's unique properties are derived from carbon-carbon strong chemical bonding. Here are some outstanding diamond properties:

- High hardness and wear resistance
- Chemical inertness
- Low electrical conductivity
- Optical transparency

Hence, for the past 40 years a variety of techniques have been employed to find an alternative production method for the natural diamond formation condition, which requires very high temperature and pressure. Diamond Like Carbon (DLC) is a general term given to a broad range of amorphous carbon materials that are produced by different techniques from pure PVD to different CVD processes. Several studies were implemented to employ this coating in different fields of application that are discussed in the next section.

1.1 DLC applications

DLC coatings were first employed for their mechanical properties as a hard wear resistant coating for protection and friction reduction purposes such as: in gears, bearings, extrusion die. (Figure 1) [1]. However, they cannot be used in applications at very high temperatures [2].

DLC mechanical properties, along with optical transparency, made it a good candidate as a protective layer over hard disk drives (Figure 2) [3]. Diamonds are transparent to the laser beam that is used for data transfer in hard disks.

The high density and compact atomic structure of DLC is also beneficial for CO_2 loss prevention and O_2 penetration into beverages when it is applied over the inner surface of polymeric beer bottles. This could help to prolong bottle shelf life and conserving the quality of beverages (Figure 2) [2].

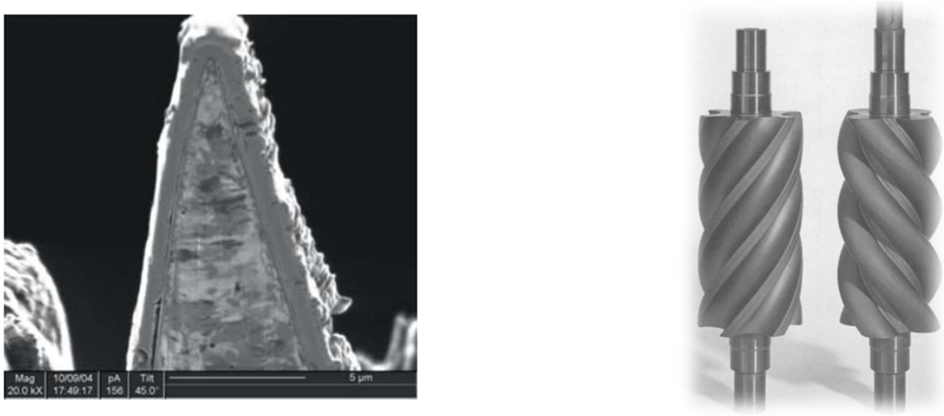

Figure 1- Examples of hard carbon coating applications. An SEM image of a DLC coated razor blade (left) and compressor screws with carbon and carbide multilayer coating (right) [1].

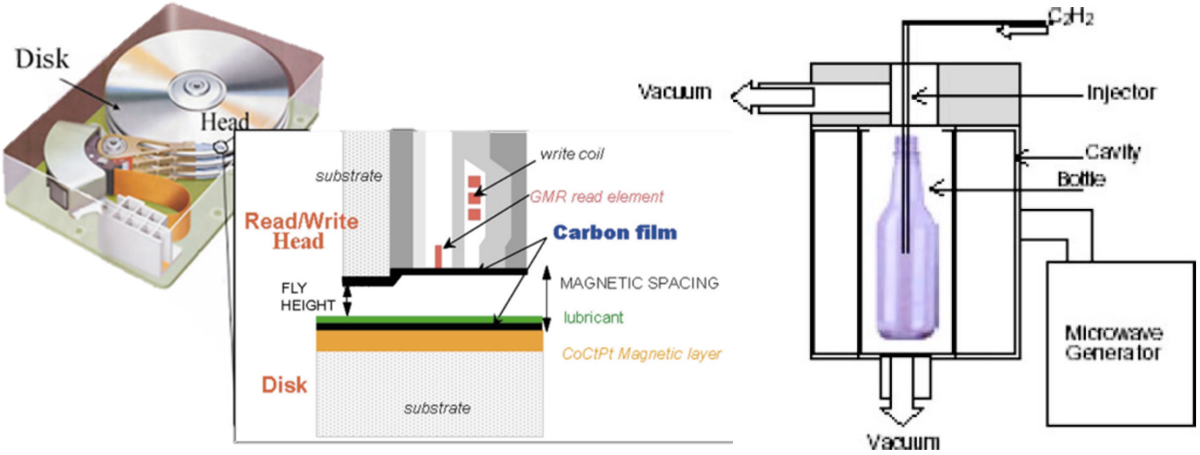

Figure 2- DLC as a transparent protective layer in hard disk drive (left) [3]. A schematic design of beer bottle inner surface carbon coating for longer shelf life [2].

This type of coating has also been studied for biomedical applications either as a wear resistant coating as in synthetic articulations (because of high mechanical properties and proper biocompatibility) (Figure 3) [4] or as a durable antibacterial coating (because of its high wear resistance and smooth surfaces that hinder the bacteria attachment and biofilm formation) [5–7].

Beside all of these unique properties and wide range of application, there are some limitations with amorphous carbon coatings, which are discussed in the section 1.2.

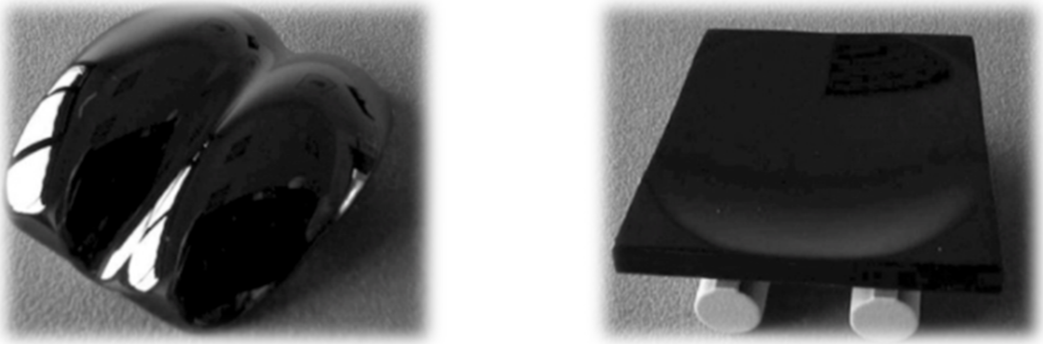

Figure 3- DLC coating over knee articulation replacement [4].

1.2 Limitations of DLC coatings

All the properties of DLC coatings come from their chemical structure, which contains a mixture of carbon atoms with sp^2 or sp^3 hybridization. A high sp^3 content of a DLC coating, which is responsible for the mechanical properties, provokes a high internal compressive stress at the same time. This restricts the coating thickness and its application in harsh mechanical conditions. This internal stress may result in low adhesion to the substrate, which results in coating delamination.

This study aims to evaluate application of optical emission spectroscopy technique as a plasma diagnostic method. This study also aims to demonstrate its potential as a monitoring tool for plasma enhanced chemical vapor deposition process of DLC coatings, in order to establish a proper model for developing a multi-layer or a functionally gradient DLC structure. These types of structures are shown to be effective in suppressing internal stresses.

The next chapter is a review about diamond-like carbon coatings, as presented in contemporary literature.

The third chapter discusses plasma diagnostic techniques, especially the optical emission spectroscopy and provides a literature review on its application for carbon containing plasma.

The chapter four is devoted to the project and describes its different parts, which are State of the problem, Materials and Methods, Results and Discussions.

Finally, chapter five is a summary of the study and the resulted conclusions along with suggestion for further studies. Supplementary information about different parts of this research is available in the appendices.

2 Amorphous carbon coatings

2.1 Diamond-Like Carbon: a general term for a wide range of amorphous carbon coatings

The four valence electrons of carbon atoms can form three different modes of chemical hybridizations (sp^1, sp^2, sp^3 as shown in Figure 4) that make the carbon to be naturally found in either allotropic form of diamond, graphite or in an entirely amorphous structure. In a diamond structure, all four valence electrons are involved in well directionally defined sp^3 orbitals. They form four strong σ bonds with their adjacent carbon atoms. In sp^2 hybridization, one of the valence electrons forms a π orbital perpendicular to the plane of the three σ bonds (as in graphite). In a sp hybridization, two of the valence electrons form two σ bonds along the X-axis, while the remaining two electrons form two π orbitals in the Y-Z plane. Each of these hybridizations results in different structures and therefore different properties in the final carbon material. Table 1 presents how different carbon materials can have quite different properties.

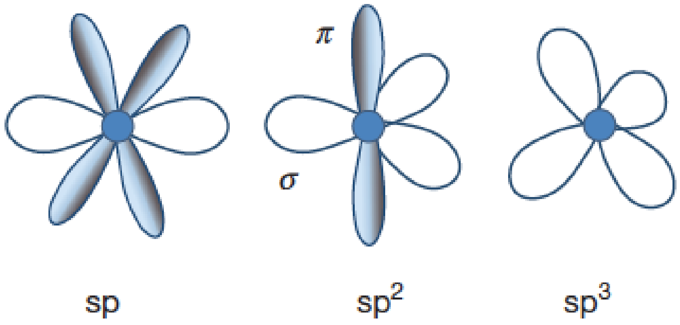

Figure 4- The three main hybridization states in carbon atoms [8].

Table 1- A comparison between Diamond and graphite properties [9,10].

Property	Unit	Diamond (sp^3)	Graphite (sp^2)
Hardness	[GPa]	90-100 *	-
Elastic modulus	[GPa]	1000 - 1200	~700 parallel to the graphite plane
Mass density	[g/cm^3]	3.515	2.267
Compressibility	[cm^2/kg]	1.7 x10^{-7} **	-
Thermal conductivity @ 298 K	[w/cm K]	~20 *	-
Optical band gap	[eV]	5.5	0
Electrical resistivity	[Ωcm]	10^{16}	10^{-2}

* Higher than any other material ** Lower than any other material

Natural diamonds are formed under very harsh conditions (high pressure and high temperature, which are naturally provided in deep layers of the earth) that are difficult to resemble for a synthetic diamond material production. Instead, different CVD or PVD techniques have been employed to produce different diamond like materials.

Synthetic diamond-like coatings are a mixture of microcrystalline diamond and an amorphous carbon phase. They usually contain considerable fraction of sp^3 hybridization. This is the reason why it is called Diamond Like Carbon (DLC). However, in practice this term covers a wide range of amorphous carbon materials from graphite (100% sp^2) to amorphous carbon (a-C) to structures that are similar to diamond (tetrahedral amorphous carbon (ta-C) with 90% sp^3). The hydrogen content of a coating (0-40%) also changes the coating properties [10–12]. The following ternary diagram (Figure 5), introduced by Jacob and Moller [13] and developed by others, depicts how sp^3/sp^2 ratio and H-content determine the final DLC structure. Table 2 shows how DLC properties may vary from that of diamond to graphite in a DLC coating family.

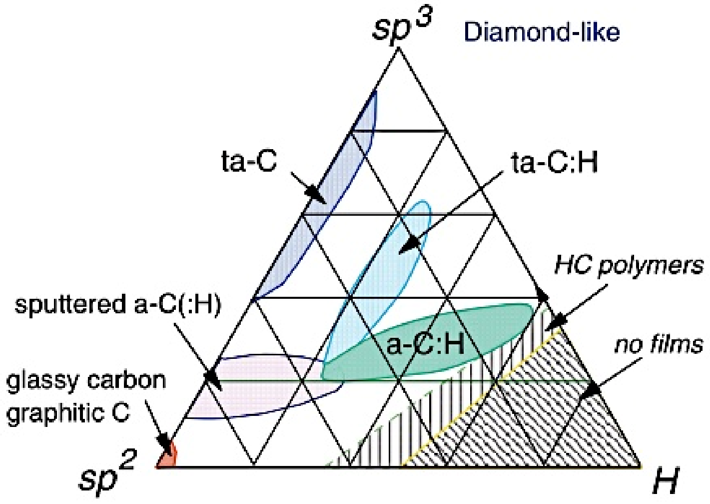

Figure 5- Ternary diagram of carbon and hydrogen depicts various type of amorphous carbon structure [2].

Table 2- The range of properties for a DLC coating [10,14,15].

Property	Diamond	ta-C	ta-C:H	a-C:H hard	a-C:H soft	Graphite
sp^3 content %	100	40-80	-	-	-	0
Hydrogen content %	0	0	30	30-40	40-50	0
Hardness [GPa]	90-100	80	50	10-20	<10	-
Elastic Modulus [GPa]	1000-1200	750	300	-	-	-
Density [g/cm^3]	3.515	3.1	2.4	1.6-2.2	1.2-1.6	2.27
Optical gap [eV]	5.5	2.5	2-2.5	-	-	0

Schmellenmeir first developed the DLC coatings in the 1950s by exciting a discharge in an acetylene medium. The term “Diamond like Carbon” first came after Aisenberg and Chabot [16]. In the 1960s, Angus in America and Deryagin in the USSR made DLC coatings throughout using thermal CVD of carbon-containing precursor gases. Then, during the 1970s, Deryagin reported a carbon coating that was produced using an electrical activating method. Then in the 1980s, low-pressure plasma enhanced CVD techniques were introduced[17]. The use of hydrocarbon plasma brings higher deposition rates comparing with carbon ions from a carbon target. A variety of different techniques (ion beam deposition, cathodic arc deposition, plasma enhanced CVD, laser ablation, sputtering, etc.) have been employed for DLC deposition. Filtered ion methods (Mass selection beam deposition (MSIBD) or filtered-arc) are also of interest since they provide carbon ion beams with narrow and controlled energy ranges [18].

2.1.1 Plasma enhanced chemical vapor deposition (PECVD) of DLC

Diamond is thermodynamically a meta-stable material. The sp^3 hybridization requires a non-equilibrium technique such as plasma deposition that facilitates the formation of coatings. This hybridization naturally needs very harsh conditions to be formed and because of this, these techniques are called plasma-enhanced deposition. Unlike the naturally formed materials, which are the thermodynamically stable state, the coatings made by plasma are in a meta-stable state. The stable form of a carbon atom at 298 K and 1 atm is in a sp^2 hybridization. However, the large required activation energy barrier for sp^3 to sp^2 transformation makes the meta-stable sp^3 C to remain stable in this condition. Aside from its high deposition rate, deposition at a lower temperature is another advantage of PECVD compared to other CVD techniques that makes it possible to deposit over a wide range of substrate materials including those of lower melting points [19].

2.1.2 DLC coating formation mechanism

In general, H abstraction from the surface is the first step in surface mechanisms, which takes place when an atomic H hits the surface and remove a bonded H atom to form a H_2 molecule. This H removal results in a free dangling bond on the surface that is a chemically active site for further reaction. The most probable consequent reaction would be bonding with another atomic H. The CH_x (x=0-3) species displacement is much slower than the H atoms because of their higher mass. However, once they arrive to the surface, they fix themselves by forming three or four bonds with their adjacent carbon atoms. The Increase of the number of bonds has a dual effect on a single atom [20]:

- More stability due to more fixation sites and
- Less stability because of increased energy, which is a result of bond stretching and bond angular distortion forces (network constraints).

The balance between these two competing forces is achieved when the average coordination number reaches the allowable degree of freedom. To describe the thermodynamically stable structure of carbon coatings, Döhler introduced how the number of constraints (N_{con}) can be found from the coordination number (m) in a random network:

- $N_{con}= m^2/2$ for $m \leq 2$
- $N_{con}= 5m/2 - 3$ for $m > 2$

So in an amorphous carbon structure one can calculate theoretical constraints number as presented in Table 3 [21].

Table 3-Theoretical coordination and resulted number of constraints in a hydrogenated amorphous carbon structure

x_i	Atom	Coordination number (m)	Number of constraints (N_{con})
x_H	H	1	0.5
x_{sp2}	sp^2 bonded C	3	4.5
x_{sp3}	sp^3 bonded C	4	7

Assuming an average coordination number of 3 for an amorphous network, Döhler achieved a condition for a complete constraint network (Eq. (1)).

$$\sum x_i N_{con_i} = 3 \qquad (1)$$

According to Eq. (1) and data on Table 3, one can conclude

$$0.5x_H + 4.5\, x_{sp2} + 7\, x_{sp3} = 3, \qquad (2)$$

knowing that

$$x_H + x_{sp2} + x_{sp3} = 1 \qquad (3)$$

At the end, the range of composition over which a fully constraint network (FCN) of amorphous carbon structure can exist can be calculated using this equation:

$$\frac{x_{sp3}}{x_{sp2}} = \frac{sp^3}{sp^2} = \frac{8x_H - 3}{8 - 13x_H} \qquad (4)$$

This equation determines the sp^3/sp^2 ratio at which the number of bonds is equal to the number of degrees of freedom. Lower sp^3/sp^2 ratio results in under-constraint soft polymeric (floppy) structure while the greater ratio brings about over-constraint under stress network. Angus developed a graph for the FCN model and evaluated it with the result of other researchers (Figure 6) [11]. The over-constrained and under-constrained regions and some crystalline and polymeric examples are marked on the graph below.

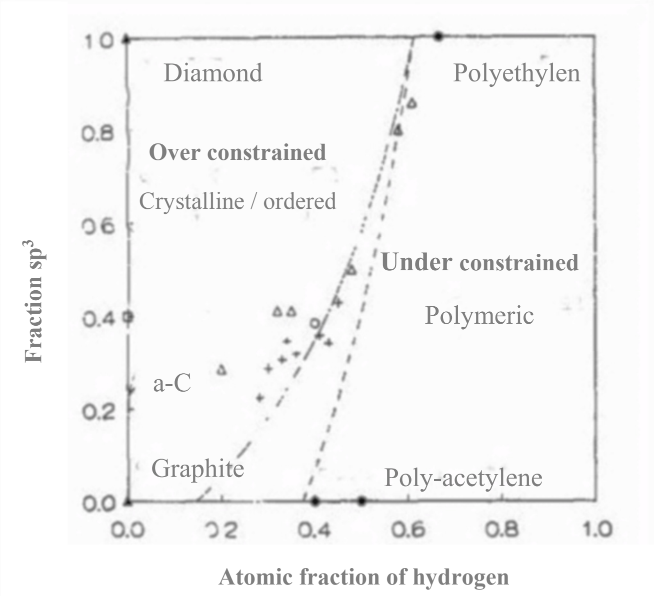

Figure 6- The fully constrained network (FCN) model for hydrogenated amorphous carbon structures. Proposed by Angus [11]. Two curves are based on different assumptions on clustering of sp^2 carbon atoms.

Different mechanisms have been proposed on DLC coatings growth. Keudell explained the growth as a two-step adsorption process. At the beginning, CH_x species are adsorbed physically to the substrate surface. Then, subsequent impinging ions provide required energy to pass the activation barrier for a chemical bonding to the surface [22]. However, it is agreed that excessive energy of the bombarding atoms leads to gradual suppression of sp^3 bonding.

According to Lifshitz, DLC deposition process is not a surface process. Instead, it is a shallow implantation (sub-plantation) process in which incident atoms enter subsurface sites. Lifshitz believes that subplantation process evolves in the following steps [23]:

- Penetration of carbon species into sub-surface layers
- Local stress induction due to penetrating atoms
- Evolution of a pure carbon layer during sputtering
- Coating growth on successive bombardment

Robertson made a link between sp^3 hybridization of carbon and local intensity of carbon atoms. He suggests that high energetic ion flux causes deep penetration and a metastable increase in local density that is a favorable condition for sp^3 hybridization [12].

Table 4 shows the evolution process for the mechanisms proposed for DLC growth:

Table 4- Proposed mechanisms and models for hydrogenated amorphous carbon coating.

Who	When	What
Spencer *et al.* [24]	1976	sp^3 sites arise from preferential sputtering of sp^2 sites by impinging high energetic ions
Döhle[20]	1980	Fully constrained network (FCN)
Weissmantel[25]	1982	sp^3 sites arise from the thermal shock-wave of the ion cascade DLC resulted from the transient high pressure-high temperature spikes caused by impact of energetic ions
Windishmann	1987	Ion-peening compressive stress
Lifshitz et *al.*[26]	1989	Sub-plantation (Low energy implantation), in which ions enter subsurface sites. sp^2 carbon atoms are displaced into sites where they became sp^3 coordinated
McKenzie *et al.*[27]	1991	sp^3 bonding stabilized by compressive stress (from ion bombardment and ion-peening), which moves a-C into the stability domain of diamond
Robertson[12]	1994	Formation of meta-stable sp^3 hybridization as a result of local density increase

2.1.3 Compressive stress in DLC coatings

Deposition of DLC coatings with a high sp^3 fraction encounters some obstacles such as development of high compressive internal stress during coating deposition. A compressive stress of 10 GPa is reported in a coating with 90% sp^3. Lifshitz addressed some technical issues about DLC coatings. Among them, he mentioned the problem of internal compressive stress that limits the coating thickness[18].

Atomic or ion peening is introduced as the source of internal compressive stress, which happens when a coating is deposited under bombardment of high energetic atoms or ions. In this condition, ions enter the spaces in the coating that are not large enough for them. Therefore, This results in the development of compressive stress in macroscopic scale during the film growth [28]. Bilek and McKenzi presented the following graph (Figure 7) to describe the effect of ion energy on internal stress level [29]. The graph shows how the film stress is related to the energy of incident ions. A thermal spike appears upon the incidence of energetic ions. The quench time of these spherical thermal spikes is proportional to the square of their radius [30]. The compressive stress firs appear when the ions get enough energy to penetrate into the surface. It increases gradually with respect to the ion energy and reaches a maximum. Until this point, the quench time is too short for relaxation. Afterward, the larger spikes provide longer quench time that let the structure to relax itself by consuming excess energy.

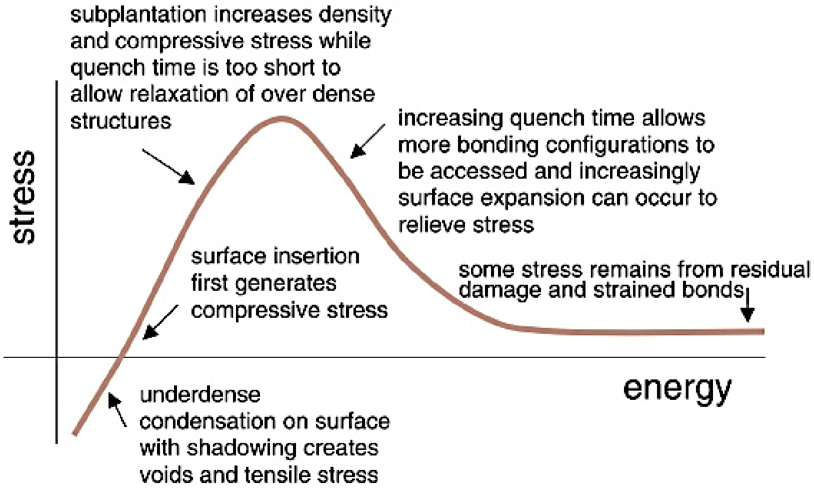

Figure 7- stress-energy curve describes how ion energy affect internal the stress level in a coating [29].

Therefore, ion energy plays an important role in the structure and properties of DLC coatings. The source of ion energy in a PECVD deposition process is the ion acceleration by applying a bias voltage. This parameter, along with other process parameters, has been studied in this research.

2.2 Conclusion

The term DLC refers to a wide range of amorphous carbon structures with a wide range of properties. Therefore, it is important to determine what type of DLC is produced as a result of a deposition process. Proposed mechanisms for DLC deposition help to better understand the growth phenomena in each type of DLC deposition processes. The PECVD process, which usually uses hydrocarbon gases as precursor, results in a hydrogenated amorphous carbon (a-C:H) as the dominant DLC structure. The ion energy has a key role in this deposition process and determines the final coating structure.

3 Plasma and plasma diagnostic methods for carbon containing plasma

Receiving enough energy, the materials state changes from a solid into a liquid and then into a gas. If one continues to supply energy into a gas medium, the collisions between atoms and molecules and free electrons, result in dissociation, ionization or excitation of them. Consequently, a mixture of negatively charged electrons, positively charged ions, radicals and neutral species will be produced. This is the plasma state. This is the reason why plasma is usually called the "fourth state of matter" after solid, liquid and gas. The required energy for the formation of a plasma medium could be provided from different sources of energy (flames, discharge, electromagnetic waves, lasers, etc.).

Table 5- General categories of plasma.

	Low-temperature Plasma (LTP)		High-temperature Plasma (HTP)
	Non-thermal LTP	Thermal LTP	
Related Temperature	$T_{ion} \approx T_{gas} \approx 300K$ $T_{ion} \ll T_e \leq 10^5K$	$T_e \approx T_{ion} \approx T_{gas}$ $T_{all} \leq 2 \times 10^4K$	$T_e \approx T_{ion} \approx T_{gas}$ $T_{all} \geq 10^6 - 10^8K$
Electron density	$n_e \approx 10^{10}m^{-3}$	$n_e \geq 10^{20}m^{-3}$	$n_e \geq 10^{20}m^{-3}$
Degree of ionization	$10^{-8} - 1$		≈ 1
Pressure	$10^{-6} - 1\ bar$		$\geq 1\ bar$
Example	Low-pressure glow discharge	Arc plasma at atmospheric pressure	Fusion plasma

As stated in Table 5, plasma mediums are categorized in two different groups of high and low temperatures, based on the energy level of electrons and ions inside plasma.

The low temperature non-thermal plasma is a non-equilibrium medium in which electron temperature is much more than ion/gas temperature. These energetic electrons are responsible for the dissociation of large molecules.

Different sources have been employed for plasma generation. Among them, the microwave and the radio frequency discharge plasma are frequently used in laboratories and industrial application for the purpose of materials surface treatments. They generate a chemically active atmosphere while the medium temperature is kept low. In this way, plasma is widely employed to boost a CVD process and it is called plasma enhanced chemical vapor deposition (PECVD).

To explanation a plasma medium (in terms of chemistry and kinetics) one needs to determine as accurately as possible, as many parameters as possible, with the help of as many independent diagnostic techniques as possible. The main parameters that are usually studied in plasma characterization are [31,32]:

- Chemistry of plasma.

  Employed precursors and their degree of ionization (DI) inside plasma.

- Temperature and density of plasma components.

  Electron density (n_e), ion density (n_i), and their related energy distribution function.

- Magnetic and electric field strength.

Based on different physical approaches, a variety of techniques have been employed to study plasma states. Aside from macroscopic properties of plasma (color, pressure, etc.), several plasma diagnostic methods have been used to study carbon containing plasma such as: electrostatic probes [33–35], optical emission spectroscopy, optical absorption spectroscopy [36–39], and mass spectroscopy [40–42] (Table 6). Each of these plasma characterization methods has pros and cons. For instance, the Langmuir probe is a practical method for electron energy distribution analyses inside a plasma medium. However, it is an intrinsic characterization method, which means that it somewhat perturbs the plasma environment. Another example is the OES method. The OES extrinsically probes the plasma and provides information about identity, temperatures (electronic, vibrational, and/or rotational) and density of the excited species. Although being advantageous at first sight, The OES requires to make some hypotheses related to the energy distribution of the plasma species as well as the mechanisms of excitation[43,44].

Table 6- The main group of plasma diagnostic methods and their capabilities for plasma measurements.

Diagnostic group	Technique	Purpose of study	Ref.
Electric probe			
Langmuir probe		Electron temperature (T_e) Electron density (n_e) Electron energy distribution (EED) Ion density (n_i)	33,34,45–47
Faraday cup		Ion average energy level Ion energy distribution (IED)	35,48–50
Optical spectroscopy			
Emission spectroscopy	Optical emission spectroscopy LIF[1]	Optically active species characterization Electron Temperature (T_e) Plasma Temperature Rotational/vibrational Temperature Species concentration	36,37,42,51–55
Absorption spectroscopy	Infrared (Diode laser, FTIR[2]) TDLAS[3] BAS[4]	Characterization of molecular species (except homo-nuclear di-atomic molecules) Optically active species characterization Rotational/vibrational Temperature	37–39,56–58
Mass spectroscopy			
	QMS[5] TIMS[6] PIMS[7]	Ion characterization Ion energy measurement	17,40–42,59,60

---

[1] Laser induced fluorescence spectroscopy
[2] Fourier Transform Infrared
[3] Tunable infrared diode laser absorption spectroscopy
[4] Broadband Absorption Spectroscopy
[5] Quadrupole Mass Spectroscopy
[6] Threshold Ionization Mass Spectrometry
[7] Photo-Ionization Mass Spectrometry

This study was first based on the use of electrical probe and optical emission spectroscopy (OES) as plasma diagnostic methods. But after some preliminary experience it was finally decided to focus on the OES technique. Section 3.1 is dedicated to the OES techniques. However, the concept of plasma diagnostic using electrical probes and the details of its application in this study are presented in Appendix C.

3.1 Optical Emission Spectroscopy (OES)

Optical emission spectroscopy (OES) is a non-intrusive and easy to use technique to study plasma properties. OES is used to analyze the light emitted from plasma. This light is a result of plasma species transition from an excited state into a lower energy state or ground state. In a single atom, there are some discrete well-known electronic energy levels. However, in a molecule there are sub-electronic states, which are vibrational and rotational energy levels (Figure 8) that make the emitted photons to deviate from their original energy levels. This is the reason why one observes a series of spectral lines for an electronic transition of a molecule while there is just a single emission line for each specific transition of an atom. The vibrational and rotational states arise from the relative movement of atoms nuclei with respect to each other. Every electronic transition may be accompanied by vibrational or rotational transitions that change the energy of the emitted photons into higher or lower energy levels (blue shift and red shift, respectively).

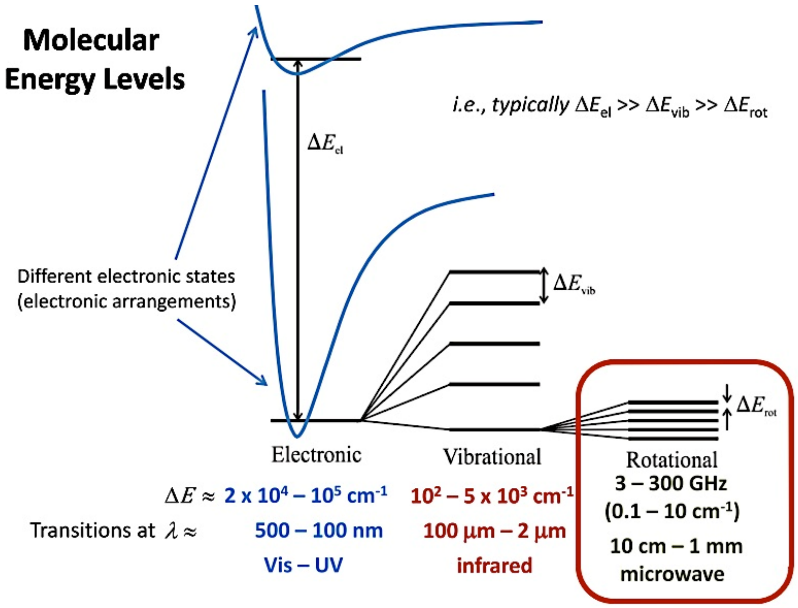

Figure 8- Electronic, vibrational, and rotational energy level in a typical molecule [61].

There are various OES studies of different types of plasma. OES studies have been widely used in the carbon containing plasma, either to study the plasma itself or to correlate plasma characteristics to the final product properties [36,55,62–64]. The following plasma characteristics are among the most frequently studied ones:

- Characterization of optically active species.
- Electron temperature measurements.
- Rotational temperature derived from molecular hydrogen and C_2 species.
- Gas temperature based on the Doppler broadening of spectral lines.
- Concentration of different species based on their emission line intensity using an actinometry method.

Among them, the last two concepts were employed in this project and will be discussed in detail in the following sections.

Table 7 summarizes reported optically active plasma species related to plasma-assisted carbon coating deposition or carbon nanotube formation, which have been observed by the OES method.

Table 7- Frequently studied hydrocarbon plasma species by optical spectroscopy.

Specie	Electronic Transition	Band location (nm)	Ref.
C_2 Swan system	$d^3\Pi_g \rightarrow a^3\Pi_u$	516	38,54,65,66 67
C_2 Mulliken system	$D^1{\Sigma_u}^+ \rightarrow X^1{\Sigma_g}^+$	231	38 67
Other C_2 system	-	432.58	54
C_3	-	405	54
CH	$A^2\Delta^- \rightarrow X^2\Pi_r$	431	36,55,64,66,68 67
H_2	$G^1\Sigma_g^+ \rightarrow B^1\Sigma_u^+$	463	36,55
	$3p^3\Pi_u \rightarrow 2s^3\Sigma_g$	602	55
H_α	3d ➔ 2p	656	41,42,55,64,66,68
H_β	4d ➔ 2p	486	55,64,68
H_γ	5d ➔ 2p	434	55,68

.

3.1.1 Emission line profile and gas temperature measurement

The gas molecule dissociation in a plasma medium can take place as a result of either electron impact dissociation or thermal dissociation, according to the plasma nature.

Therefore, electron energy level and gas temperature (T_g) are the controlling parameters for a plasma medium. The concentration of plasma species can be strongly affected by either of these two factors [69]. This is the reason why these two parameters are usually studied in a plasma diagnostic analysis.

Knowing the nature of discrete energy levels in atomic structures, the emission spectrum of a species should include some narrow lines that appear at pre-defined wavelengths. Instead, in practice, there are some wide bands. The full width at half maximum (FWHM) of a line ($\Delta\lambda_{FWHM}$), which is a result of the photon frequency shift and broadening mechanisms, is a characteristic of a plasma medium. The following phenomena are the main broadening mechanisms in plasma spectroscopy that result in the broadening of emission lines [43]:

1- **Natural broadening**. It arises from the uncertainty in the energy of the states involved in the transition. It is not significant in atomic spectroscopy.

2- **Doppler broadening.** It is the most prominent broadening mechanism for atomic spectra in the UV-visible range. It arises from the thermal motion of atoms with a velocity of V in different directions, which affect the received frequency by the spectrometer.

3- **Collisional broadening**. Electron energy level in an atom or ions can be distorted as a result of frequent collisions with other particles, which results in the broadening of the related spectral line. Collisional or pressure broadening is not significant in low-pressure plasma spectroscopy.

A combination of all of the above mechanisms can also be involved. The natural broadening and collisional broadening mechanisms are negligible in spectroscopy of atomic species in low-pressure plasma, which is the case in the most PECVD processes of DLC coatings. Therefore, the Doppler broadening mechanism can be used for temperature estimation using Eq. (5). This temperature for such a PECVD process is supposed to be in the range of some thousands of Kelvins [70,72].

$$\frac{\Delta\lambda}{\lambda_0} = 2\sqrt{2ln2\frac{kT}{mc^2}} = 7.16 \times 10^{-7}\sqrt{\frac{T}{m}} \qquad (5)$$

Where $\Delta\lambda$ is the FWHM around the center wavelength of λ_0 resulted from the Doppler effect. m represents atomic mass, c represents light velocity and T is the gas temperature.

The Doppler broadening mechanism is significant for hydrogen atoms when compared to other plasma particles, since they are the lightest species [70,71]. Broadening of the H_2 line has also been used to estimate translational gas temperature [72].

3.1.2 Actinometry measurements

The concept of the actinometry was first introduced by Coburn in 1980 [73]. It is a technique used to estimate relative densities of a ground state species in reactive plasma using OES measurements. The intensity of each spectral line in an OES result is proportional to the excited state population of that species. This is usually less than 10^{-4} of its population in the ground state that is responsible for the deposition process [70]. The actinometry method helps to measure the total concentration of each species based on the concentration of an inert gas, which is known as actinometer.

In actinometry, a small amount of an inert gas (usually argon), which has similar excitation energy levels to that of the probed species, is used as a reference. The relative intensity of the probed species over the intensity of the actinometer is related to the relative concentration of these two species in their ground states. One can then estimate the total population of the desired species, knowing the concentration of the actinometer. The selection of an actinometer gas must be based on the following assumptions:

- The actinometer should not affect the plasma (usually actinometer concentration is around 1% of the total gas mixture).
- Both the probed species and the actinometer should be excited from the ground state via a single electron impact excitation.
- Both species should have a similar energy threshold for excitation.
- The predominant de-excitation process should be a radiative relaxation transition, which occurs in low-pressure plasma.

Eq. (6) relates H atom concentration to measured spectral intensity ratio of hydrogen and that of Ar [72,74]:

$$\frac{[H]}{[Ar]} = \frac{x_H}{x_{Ar}} = F\frac{k_e^{Ar*}}{k_e^{H\alpha}}\frac{\upsilon_{Ar*}}{\upsilon_{H_\alpha}}Q_T\frac{I_H}{I_{Ar}} \qquad (6)$$

This technique has been employed for carbon containing plasma processes by several authors [72,74]. It has been shown that one of the transitions of Ar atoms (4p) (4p→ 4s at 750 nm) has the same excitation threshold as H (n=3) excited state, when excited from its ground state [36,74]. The same Ar line also has been used for CH concentration measurements (Table 8).

Table 8: Argon as an actinometer for density measurement of different plasma species.

Plasma species	Proper Actinometer	Ref
CH ($A^2\Delta$ to $X^2\Pi$) at 431.4 nm	Ar @750.4 nm with energy threshold of 13.5 eV. While CH excitation energy threshold is 12.2	36
H_β : H (n=4 to n=2) at 486 nm	Ar @750.4 nm with energy threshold of 13.5 eV. While H(n=4) excitation energy threshold is 12.75	36
H_α: H (n=3 to n=2) at 656 nm	Ar ($4p \rightarrow 4s$) lines: $2p_1 \rightarrow 1s_2, \lambda = 750.3\ nm$, excitation energy level: 13.48 eV $2p_9 \rightarrow 1s_5, \lambda = 811.5\ nm$, excitation energy level: 13.05 eV	74

3.2 Conclusion

The above-mentioned techniques help to extract different types of data from OES results to characterize the plasma medium. The concept of estimating a gas temperature from the shape of its spectral line was introduced in this section. Then, the basics of actinometry as a measurement tool for plasma species concentration was discussed. These plasma diagnostics help to understand plasma nature and can be employed to find a correlation between plasma parameters and resulted DLC coating properties.

4 Project

4.1 State of the problem

Referring back to the DLC structure and its formation mechanism as described in chapter 1, the level of internal compressive stress increases as the structure of the amorphous carbon coating gets closer to that of diamond. This compressive stress is responsible for high hardness and Young modulus of the coating on one hand, but on the other hand, it also decreases the coating adhesion to the substrate. A stress level of 5-10 GPa has been reported depending on the type of DLC [14]. Figure 9 depicts an example of a DLC coating over a silicon substrate that is partially delaminated to relax its internal compressive stress.

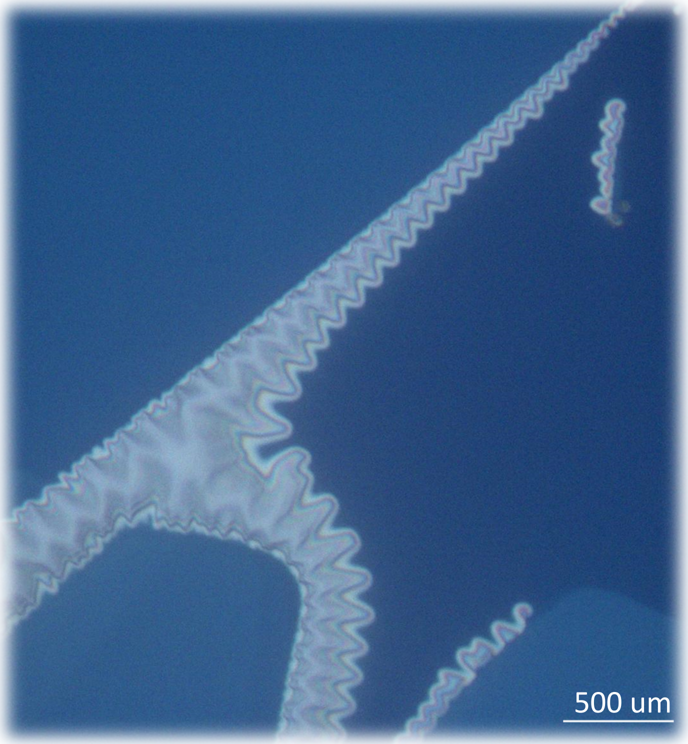

Figure 9- An optical microscopy image of a typical DLC coating delamination as a result of high internal compressive stress (coating is deposited by the author).

Different approaches have been studied to overcome this limitation such as: Annealing [75,76], doping with different types of metallic elements [77–79] and multi-layer or structurally gradient DLC [80–82]. These approaches can be divided into two main groups [83]:

- Doping the carbon coating to suppress the internal stress by changing the uniformity of the over-constraint DLC structure. Table 9 presents the main group of dopants and previous research in this regard.
- A multi-layer or a gradient structure. Some previous research is presented in Table 10.

Table 9- Different types of dopants have been used in various amorphous carbon coatings.

Dopant elements		Role	Ref.
Inert to carbon metals	Ag Cu	Island formation of dopants due to low chemical affinity with carbon atoms. The nanometer sized segregates can reduce the strength and the directionality of carbon bonds that are responsible for film stress and hardness	[6,77–79]
Carbide forming metals	Ti W Ni Ta	Increase DLC coating adhesion by increasing the integration to its metallic substrate	[64] [84] [85] [86]

Table 10- Examples of multi-layer and gradient DLC coatings.

Dopant elements	Role	Ref.
Multi-layer coatings & Gradient coatings	A multi-layer structure, in thick coating, restricts crack propagation and thus increases the coating toughness. a-C:H / a-$Si_{1-x}C_x$:H	80,87
	To change the sp^3/sp^2 ratio through the coating thickness.	81,82
	Metal carbide as buffer layer: - To induce chemical or mechanical bonding between the substrate and the coating - To provide a transitional modulus and thermal expansion coefficient between that of the DLC and that of the substrate	88
	Zr-ZrC/ZrC-DLC	89

The gradient structure is known for the gradual change of structure and therefore the properties through the thickness. One can tailor a DLC coating according to the desired application. For example, one can obtain a higher hardness at the outermost surfaces whilst keeping stronger adhesion to the substrate. The benefit of a gradient structure is that it bears no interface compared to a multi-layer structure. An interface is a thermodynamically high-energy region in a coating structure that may potentially be a weak point.

To design a gradient coating, it is necessary to know the correlation between the structure of nanocoating and the plasma process parameters. Several researchers have studied the effects of process parameters such as: plasma power and pressure. on the properties of DLC coatings [90,91]. However, the relationship between such parameters and plasma characteristics, which directly affect the structure, differs from one reactor to another depending on the configuration of each reactor. Consequently, reproducing identical coatings in different plasma setups require to be done by using a trial and error procedure. One avenue to overcome this problem consists of correlating some plasma characteristics with the DLC coating properties.

Several plasma diagnostic methods have been used to study carbon containing plasma; like electrostatic probes [33–35], optical emission and absorption spectroscopy [36–39], and mass spectroscopy [40–42]. Each studies a specific aspect of plasma and has its own advantages and disadvantages. The Langmuir probe technique is a practical method of evaluating electron energy distribution inside plasma. The OES technique studies plasma emissions. While both techniques are easy to apply, the first is however an intrusive one that may affect plasma characteristics [43]. There are numerous studies on optical spectroscopy of carbon containing plasmas used either for carbon nanotube production or amorphous carbon coating deposition [36,55,62–64]. The knowledge gained from these publications allows the use of OES as a tool to control the process of DLC coatings through PECVD.

4.2 Hypothesis

The idea is to employ the OES as a plasma online monitoring tool and to establish a correlation between the deposited DLC coating properties and both the independent experimental parameters (plasma power, pressure, precursor gases, etc.) and the data from the OES, which comes from plasma medium. There are some studies on finding correlation between coating properties and experimental parameters [90,91]. However, the majority of these studies considers plasma medium as a black box and has not dealt with plasma characteristics in their models. Therefore, to establish a deposition condition that could be used in any laboratory with any PECVD reactor, one needs to replace experimental parameters with plasma parameters in our model. These plasma parameters can be acquired from different plasma diagnostic techniques. Such a correlation helps to predict future DLC properties based on plasma characteristics independent of process parameters, which are the reactor dependent parameters. This model can then be employed in any other reactor of similar coating processes to design a coating deposition or as a process control tool.

4.3 Objectives

The general objective of the present study is to compare both the PECVD process parameters and OES data as a predictive tool to monitor the DLC structure and its mechanical properties. This will be done by correlating either of the plasma process parameters or the OES data with the DLC structural and mechanical properties through a partial least square analysis.

The second object is to evaluate the possibility of replacing experimental parameters (process parameters) with the related OES derived variables, knowing that a part of the process parameters effects on the plasma medium will be reflected through the OES results.

Finally, it is desired to design and to monitor a gradient deposition process using this developed model.

Section 4.4 describes the plan of experiments designed in order to realize these objectives.

4.4 Materials and methods

4.4.1 Plasma reactor

Amorphous carbon coatings were deposited using an inductively coupled radio frequency PECVD reactor (FLR1200, Plasmionique Inc., Varennes, QC, Canada) over silicon wafers. Figure 10 depicts a schematic setup of the plasma reactor. Methane was used as the source of carbon and hydrogen. A separate LF power supply was employed to induce ion acceleration toward substrates by applying a self-rectified negative bias voltage to the sample holder (as the cathode) with respect to the chamber wall (as the counter electrode). A UV-Vis spectrometer equipped with a 300 lines per mm grating (HR4000CG-UV-NIR, Ocean Optics Inc. Dunedin, FL, USA) was used to record the UV-Visible spectra between 200 and 1100 nm with a spectral resolution of 0.5 nm. The entrance aperture was set to 5 micrometers.

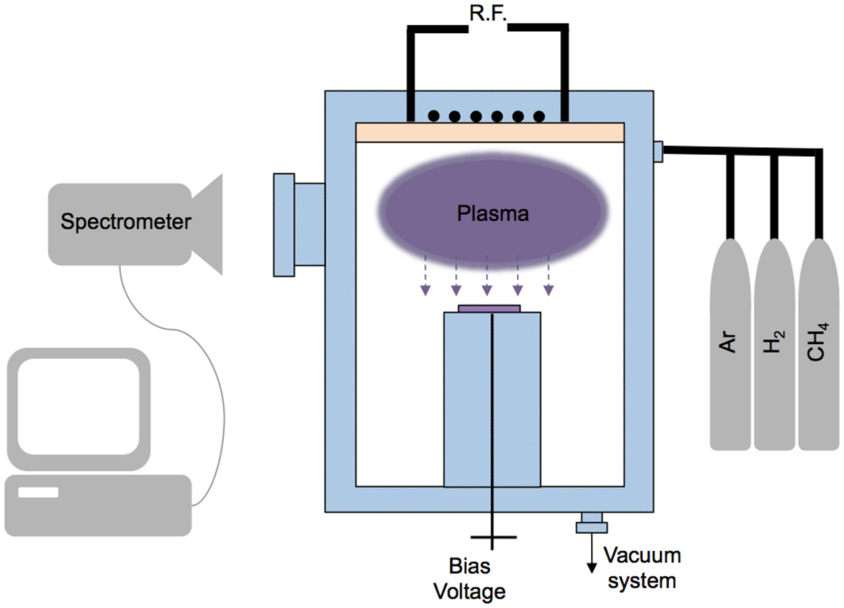

Figure 10- Schematic set up of the plasma reactor and the plasma diagnostic assembly.

4.4.2 Substrate

Silicon wafer has been widely used as a substrate for DLC deposition mainly because the fact that both Si and diamond have similar atomic structure that facilitate DLC deposition. Here the Si wafer was employed as the substrate (thickness: 500 µm, orientation (100) ±0.5 degree, polished). It is clear that in case of using another type of substrate, it is also necessary to study the substrate effect on final DLC properties.

4.4.3 Pre-deposition process

Silicon substrates were wiped and rinsed with acetone for contamination removal. Then, they were fixed over the substrate holder (using conductive carbon tape) in such a way that ensures proper electrical conductivity between the substrate and samples during plasma processes.

Argon etching

Ar plasma etching (at 100 W, 20 sccm, 50 mTorr, -100 V for 15 min) is then used to remove contaminations in a molecular level from the substrate surface.

Hydrogen etching

Bombarding the substrate by hydrogen atoms helps to activate the surface by removing hydrogen atoms from the surface and leaving some dangling bonds. Now these bonds are ready for further chemical reactions. Hydrogen etching (at 100 W, 10 sccm, 50 mTorr, -150 V for 15 min) was carried out prior to deposition.

DLC deposition

Methane and ethane are frequently used in PECVD of DLC, as a source of carbon and hydrogen. In current study, a constant flow of 7 sccm of CH_4 provided the required carbon source to build-up the diamond-like coating during 30 minutes of deposition. Following experimental parameters will be manipulated during DLC depositions:

1. Plasma RF power (P), which is the energy source for gas dissociations, ionization and plasma formation.
2. Plasma power mode (M)- either continuous or pulse mode at 100Hz and duty cycle of 50%.

3. Pressure (p)- the total pressure of the plasma chamber is measured using a Baratron-MKS system and controlled automatically by changing the speed of the turbo molecular pump and the state of the outlet valve.
4. Bias voltage (V_b), which is applied to the substrate holder and is responsible for the ions acceleration toward the substrate.

Determination of deposition parameters

A series of DLC coatings were deposited based on the above-mentioned four experimental parameters at two different levels (high / low), as described in Table 11. This range of values has been determined after carrying out several preliminary tests and it allows the deposition of DLC coatings with a variety of structural and mechanical properties.

Table 11: The range of experimental parameters employed for DLC deposition.

	Plasma Power	Plasma mode	Pressure	Bias voltage
Unit	[W]	-	[mTorr]	[V]
Label	P	M	P	V_b
Low (-)	100	0 for Continuous	10	-50
High (+)	300	1 for Pulse mode (at 100 Hz)	30	-200

4.4.4 Design of experiments

A fractional factorial design method was employed to determine the combination of experimental parameters for each deposition condition and to reduce the number of experiments [92]. Therefore, eight observations (Table 12) with three replicates were performed (training set). This allowed to build-up the training set of experiments that will be used to develop the statistical model.

A supplementary set of coatings was also deposited for evaluation of the model prediction power (prediction set) (Table 13). The combinations of experimental parameters for the prediction set were chosen among those that do not exist in the training set.

Table 12- the combination of experimental parameters for the training set of experiments.

	ID	Power P	Bias V V_b	Mode M	Pressure p^*
1	A	+	+	+	+
2	B	+	+	-	-
3	C	+	-	+	+
4	D	+	-	-	-
5	E	-	+	+	-
6	F	-	+	-	+
7	G	-	-	+	-
8	H	-	-	-	+

* Pressure is the confounded factor with interaction generated by p=PxM.

Table 13- The combination of experimental parameters for the prediction set of experiments.

	ID	Power	Bias V	Mode	Pressure
1A	P1	-	-	+	+
2C	P2	-	+	+	+
3E	P3	+	-	+	-
4D	P4	-	+	-	-

4.4.5 DLC characterization methods

In prior literature, different characterization techniques have been employed to analyze DLC coating properties and most of them are concentrated on phase determination (sp^3 fraction) or evaluation of diamond like properties (Mechanical, optical gap, electrical, etc.) [93].

In this study two main approaches are considered for DLC coating characterization:

- Mechanical and physical property characterization.
- Structural analysis.

Profilometry

The thickness of the coating was measured using a stylus profilometer (DektakXT, Bruker, USA) with a force of 3 mg applied on a 12.5 μm stylus via a step-height technique.

The internal compressive stress was calculated by measuring the surface curvature before and after the deposition using the same surface profilometer and Stoney's method [94].

XPS-AES

Various structural analysis methods differ in depth resolution or lateral resolution. The result for a homogenous bulky material would be the same for all of these methods, but not for a DLC coating, which is usually non-uniform. The ternary phase diagram of DLC shows that there are two key parameters that determine final coating structure:

- The sp^3 fraction.
- The hydrogen content.

Therefore, the majority of the structural studies are focused on these two parameters [14,18]. Table 14 shows some techniques that are most frequently used to study a DLC structure [14,18].

Table 14: DLC structure analyzing techniques

Type of analysis	Technique	Studied parameter
Surface analysis	Auger electron spectroscopy (AES)	sp^3 fraction
	X-ray photoelectron spectroscopy (XPS)	
	Low and high energy ion energy loss spectroscopy (EELS)	sp^3 fraction
Radial (bulk) analysis	Transmission electron microscopy (TEM)	
	Neutron scattering analysis (ERD, NRA, RBS, NMR, etc.)	H-content, H- distribution, sp^3 fraction
	Raman spectroscopy (Visible, UV)	sp^2 phase analysis,

The structure of DLC in the present study, was studied by X-ray excited Auger electron spectroscopy (XAES) [95,96]. The D-parameter, which is the distance between the highest peak and the lowest valley in the first derivative of the C KLL Auger peak, is related to the sp^3/sp^2 ratio and its values change from about 24 eV for graphite to 14 eV for a perfect diamond structure [95,97,98]. The XAES analysis was carried out from the Auger signal acquired using a PHI 5600-ci XPS spectrometer with an Al-standard anode in the pseudo-bonding energy range of 1200-1250 eV (Physical Electronics USA, Chanhassen, MN).

4.4.6 Plasma diagnostics - optical emission spectroscopy

The light was collected by a collimator and transferred to a spectrometer (Ocean Optics Inc. model: HR4000CG-UV-NIR, 300 lines per nm grating, entrance aperture: 5um) via a 1mm core UV-Vis optical fiber. This device is capable of recording UV-visible spectra (200 to 1100 nm) with a spectral resolution of 0.5 nm. Detector calibration was carried out using a mercury-argon light source (HG1, Ocean Optics company) with the known spectral line positions. The spectra were recorded using SpectraSuite® software (Ocean Optics company). The light acquisition was done for five seconds and repeated two times at each single measurement. Measurements were carried out at every five minutes during deposition for each single coating process. Spectral studies and analysis were done either by the SpectraSuite® or the GRAMS software.

The following data were studied through recorded spectra at different deposition conditions.

Spectral line profile - FWHM

Referring back to Chapter 3, the spectral line profile carries information from the plasma medium. The width of each line is a result of photon frequency shifts, because of different broadening mechanisms. In low-pressure plasma, the dominant broadening mechanism is the Doppler effect and it is related to gas temperature as described in Eq.(5).

The FWHM of peaks of the emitted spectra, as it was recorded by the spectrometer, contains not only the spectral broadening due to the plasma related mechanisms, but also the broadening induced by the spectrometer. Therefore, it is necessary to process the spectra and to remove the “instrumental function” before using it for the gas temperature (T_g) estimation. However, the resolution of the spectrometer used to perform the experiments was not sufficient to accurately apply this procedure. Consequently the FWHM measured so far, although not allowing to calculate accurate T_g values, is nevertheless directly related to the gas temperature and may be used as a temperature probe. Accordingly, the variation in the FWHM of a single plasma species (here, H_α), at different plasma conditions, is directly employed as a plasma parameter to be used in the model.

Actinometry measurements

Actinometry is a technique to estimate relative densities of a ground state species in reactive plasma using OES measurements. According to the discussions in Chapter 3 about the actinometry measurements, the relative intensity of a probed species over that of the actinometer is related to the relative concentration of these two species in ground state.

This technique has been employed in the carbon containing plasma process by several authors [72,74]. However, the proper use of actinometry requires meeting some critical assumptions.

First, the two species must be excited from the ground state via a single electron impact excitation. Second, both species must have a similar energy threshold for excitation. In this present study, a known amount of Ar, also used for Ar-etching, was used to perform the actinometry measurements (Ar $4p \rightarrow 4s$ transition at 750 nm) [36,74]. The relative intensity of CH, H_α and H_β to that of Ar at different plasma conditions, are employed as an index of concentration for CH and atomic hydrogen. Finally, the predominant de-excitation process should proceed through radiative relaxation, which is the case in this study.

To calculate the exact value of the concentration of each species, one needs to apply the related coefficients to this ratio, as depicted in Eq. (6). Here, we are not looking for the real concentration values. Instead, we need plasma representative parameters to be included in the model. Therefore, the intensity ratios of atomic H and CH species to that of Ar were directly employed.

4.4.7 Statistical analysis

The next step is to analyze the employed parameters and the measured values, in order to determine how the data are correlated to each other. Partial Least Square Regression (PLSR), also known as Projection to Latent Structure (PLS), is a statistical method that is practical for data analyzing when there are numerous, correlated, noisy, and sometimes missing data. It extracts the latent structure of independent (X) and dependent (Y) data set by finding new coordination systems for X and Y based on vectors along which there is minimum variance between the projected observations (also known as Principal Components (PC) or Latent Variables (LV)). The PCs describe each data space (X or Y) the best. This new coordination system is calculated in such a way that it assures the highest possible covariance between X and Y spaces. Therefore, at the same time, a PLSR model describes the data structure at predictive (X) and predicted (Y) matrices in addition to the correlation between these two [99].

A PLSR model begins by following decompositions of X and Y matrices [99] (when there are N observations with K variables in X and M responses in Y):

$$X_{N\times K} = T_{N\times A}P^{T}_{A\times K} + E_{N\times K} \tag{7}$$

$$Y_{N\times M} = U_{N\times A}C^{T}_{A\times M} + F_{N\times M} \tag{8}$$

$$T_{N\times A} = X_{N\times K}W^{*}_{K\times A} \tag{9}$$

T and U are called score matrices for X and Y, respectively, and bear the A principal components of the X and Y matrices in their columns. P and C are called loading matrices. E and F are the residuals of the model for X and Y, respectively. W* is called the weight matrix of the PLSR model and contains of the combinations of X variables that gives the best prediction of Y.

In a PLSR model, the T and U matrices are calculated in such a way that a high level of correlation between them is assured. Therefore, the T is also a good predictor of Y:

$$Y_{N\times M} = T_{N\times A}C^{T}_{A\times M} + G_{N\times M} \tag{10}$$

A combination of Eqs. (3)-(5) will be used for the purpose of the process prediction:

$$Y_{N\times M} = X_{N\times K}W^{*}_{K\times A}C^{T}_{A\times M} + G_{N\times M} = X_{N\times K}B_{K\times M} + G_{N\times M} \tag{11}$$

This calculation determines the B matrix, which contains the regression coefficients. Details on multivariate analysis are presented in appendix B.

In this study the process parameters and OES data are considered as X matrix and DLC properties as Y matrix. The multivariate analysis of this study is carried out by ProMV© software (Ver. 15.02, ProSensus Multivariate). The raw data were first auto-scaled to normalize the units and the range of variables, before being applied to the PLSR model.

Both the experimental and the OES data were considered as input data to evaluate how they affect the coating properties. Several models of different X matrix with different parameters were developed to evaluate the importance and potential of the OES derived data as a monitoring tool for the PECVD of DLC.

The best model is then used to predict DLC properties using the second group of observations (prediction set of Table 13).

4.5 Results and discussion

4.5.1 DLC coating characterization

The results of different characterization techniques are presented in this section.

Only 6 out of the 8 deposition conditions (Table 12) resulted in a stable DLC coating over silicon wafer (C, D, E, F, G, and H). The deposition conditions A and B, which both have a high level of power and bias voltage (Table 12), did not result in any coating at the end of the process. The CH_x deposition and hydrogen etching are both involved in a DLC coating growth in a competitive manner [100]. The greater population of H atoms observed in A and B conditions (that will be discussed later) resulting from high plasma power, along with their high energy levels, confirms the idea that the etching rate surpasses the deposition rate, in these two sets of observations.

AES

The first derivative of Auger peak was employed for D-parameter measurement (appendix A). Figure 11 represents the measured D-parameters of DLC coatings deposited at different combinations of experimental parameters. It is related to the sp^3/sp^2 ratio in the coating. The smaller the D-parameter, the closer the structure is to that of diamond.

Internal Compressive Stress

The internal compressive stress and the deposition rate for each DLC deposition condition are presented in Figure 12 and Figure 13, respectively.

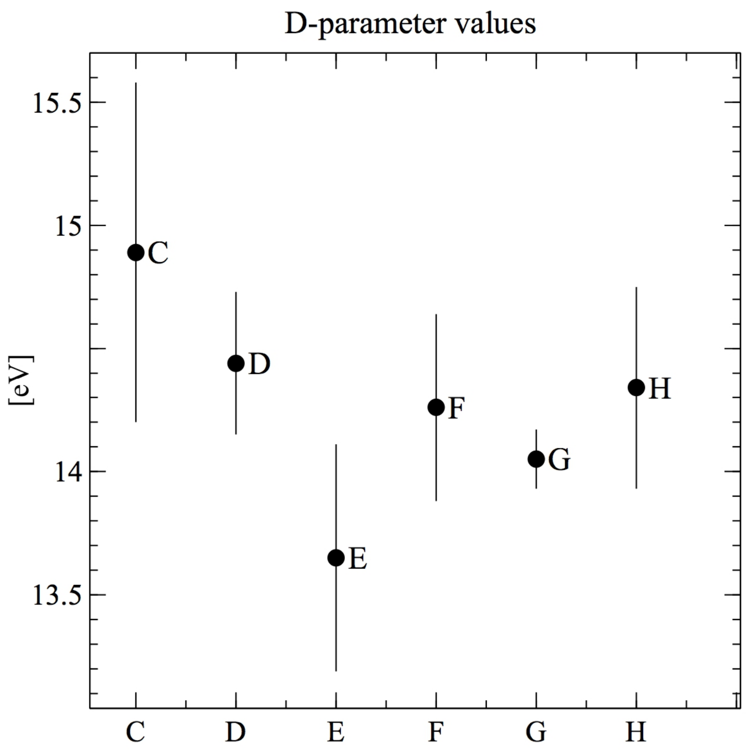

Figure 11- Measured D-parameter values for different deposited DLC coatings

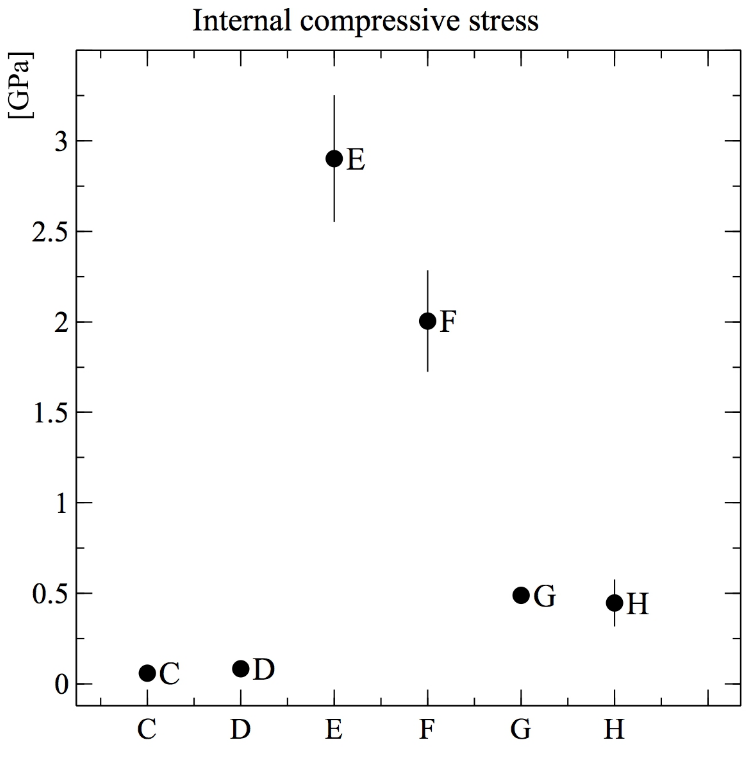

Figure 12- DLC coating internal compressive stress at different deposition conditions

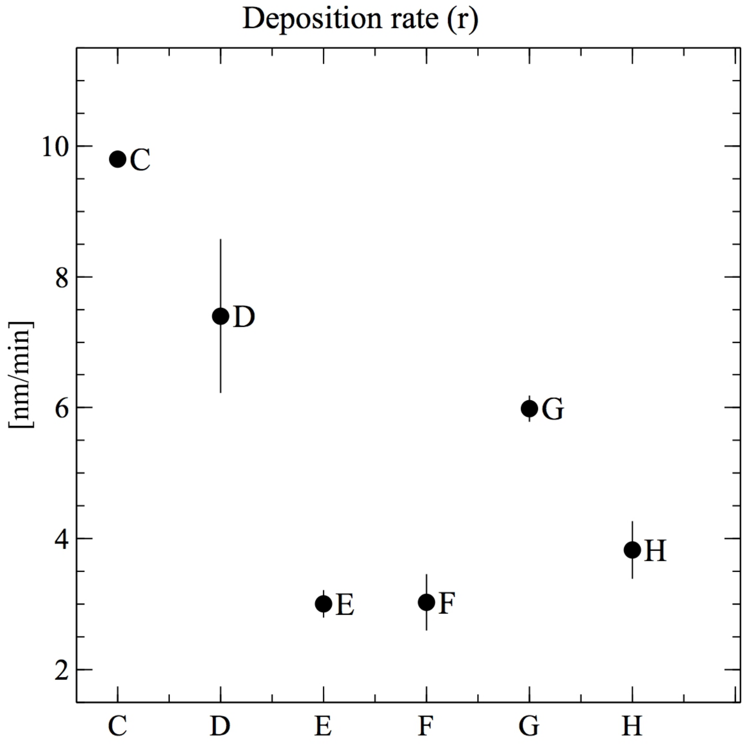

Figure 13- DLC deposition rate at different deposition conditions

As shown in Figure 11,Figure 12 and Figure 13 the deposited coatings can be categorized into three separate groups based on their properties. Group 1 includes A and B observations that do not result in a coating at the end of the process. The second group includes C, D, G and the H observations that have very low film stress and high D-parameter (graphitic properties). These coatings were coherent but soft (scratchable) and moderately adhered to the substrate. Finally, the third group includes E and F observations that have the highest internal compressive stress level. In fact, they were quite resistant against scratching and firmly adhered to the substrate. In other words, they were the most diamond like coatings in this range of deposition conditions.

Referring back to the deposition conditions from Table 12, one may found that the only experimental parameter that distinguishes groups 2 and 3 is the bias voltage (V_b). A high level of V_b in E and F observations seems to be responsible for their vastly different properties.

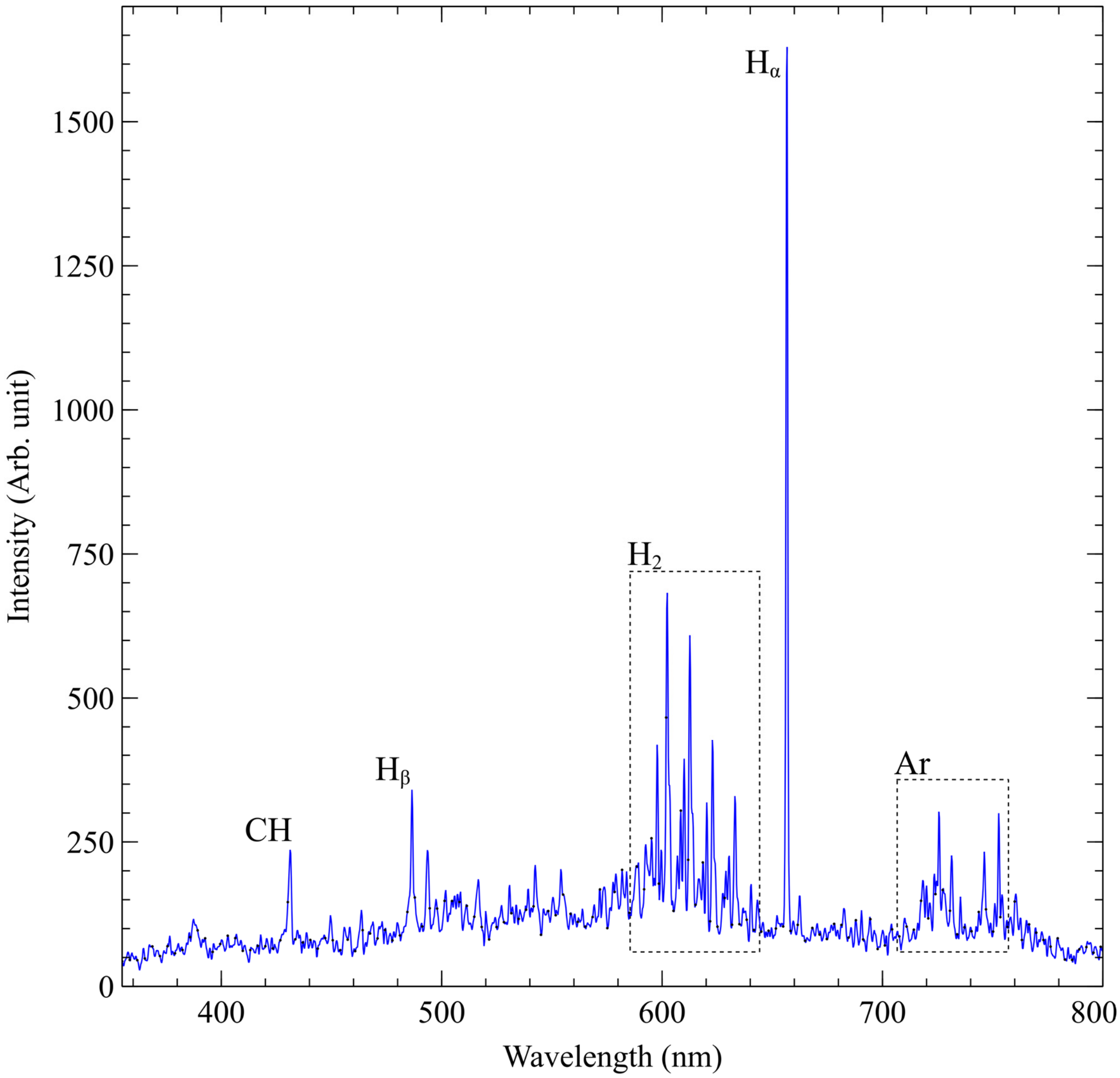

Figure 14- A typical observed spectra from CH_4 plasma. Detected lines are marked in the graph.

4.5.2 OES measurements

Depending on precursor gas composition and plasma conditions, different spectral lines can be observed in an emission spectrum [59,66,101,102]. Figure 14 shows that the emission spectrum of the investigated plasma in a methane environment exhibits features which originate from the dissociation of this molecule within the plasma environment. Indeed, H_α and H_β lines are related to the Balmer transition in hydrogen atoms. In addition, an emission line is assigned to the presence of CH moieties, indicating H removal from CH_4.

Finally, the H_2 lines are related to the recombination of two hydrogen atoms within the plasma while the Ar lines are attributed to the residual Ar gas from the pre-deposition sample cleaning step (Ar-etching).

Each species line position is in accordance with prior literature, as shown in Table 15. Spectral lines intensity and shape change according to plasma conditions. Figure 15 shows four different emission spectra related to different deposition conditions.

Table 15- Observed species, their wavelengths, transitions and upper state energy levels.

Species	Wavelength (nm)	Transition	Ref.
H_α	656	$3d \rightarrow 2p$	36,102,103
H_β	486	$4d \rightarrow 2p$	36,102,103
CH	430	$A^2\Delta \rightarrow X^2\Pi$	36,55 63,66,102
H_2 lines	600-650	$3p^3\Pi_u \rightarrow 2s^3\Sigma_g$	55,102,104
Ar lines	700-800		66

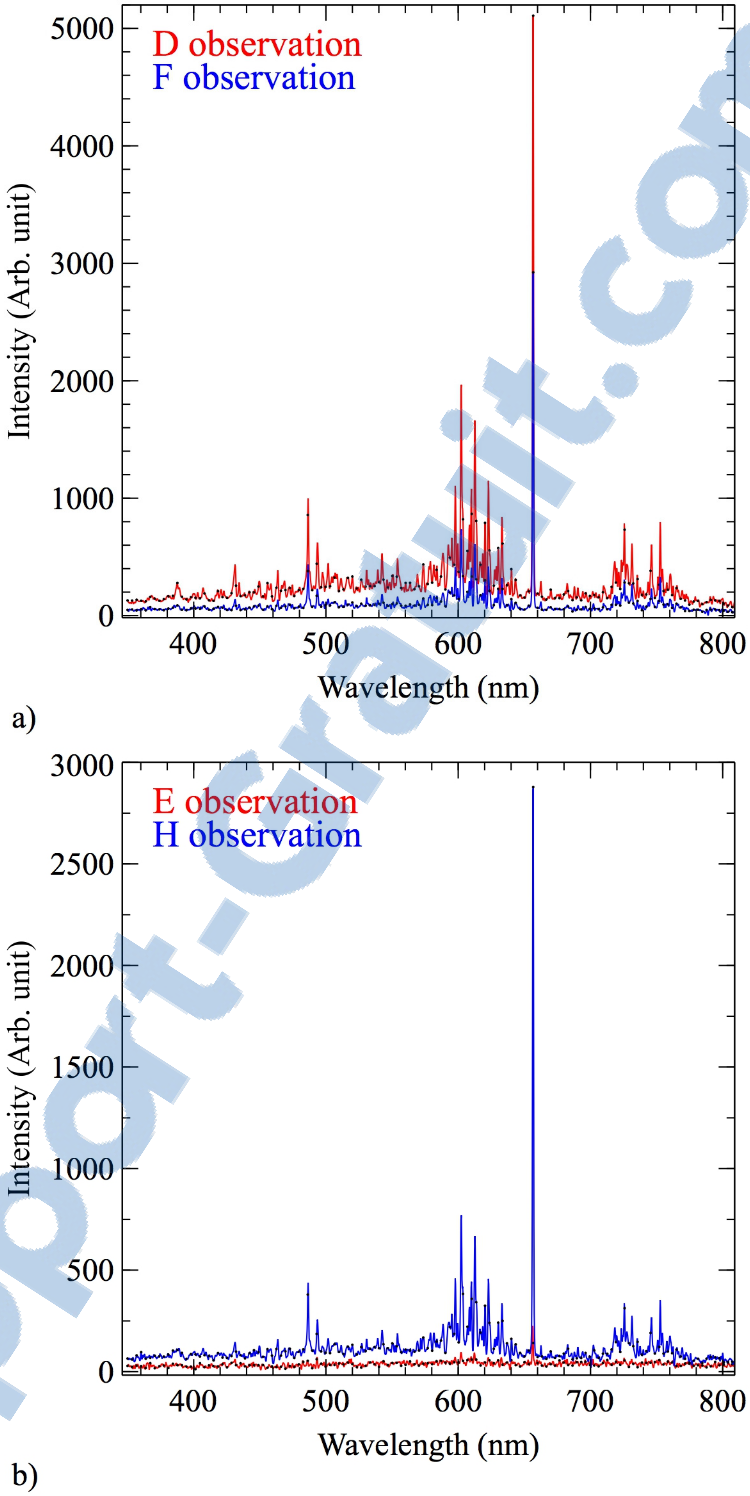

Figure 15 – Spectral line variations at different deposition conditions. a) D: high power and low pressure, F: low power and high pressure. b) E: low pressure and pulse mode, H: high pressure and continuous mode.

Processed data derived from optical spectra recorded during different observations are presented in the following sections.

Spectral line profile (FWHM)

Spectral line profiles bring energetic information from the plasma environment. The smaller emission intensity of H_β line compared to that of H_α in our observations, can harmfully affect the FWHM measurements. Therefore, the H_α line was selected for line profile analyses. Figure 16 shows the measured FWHM of H_α lines.

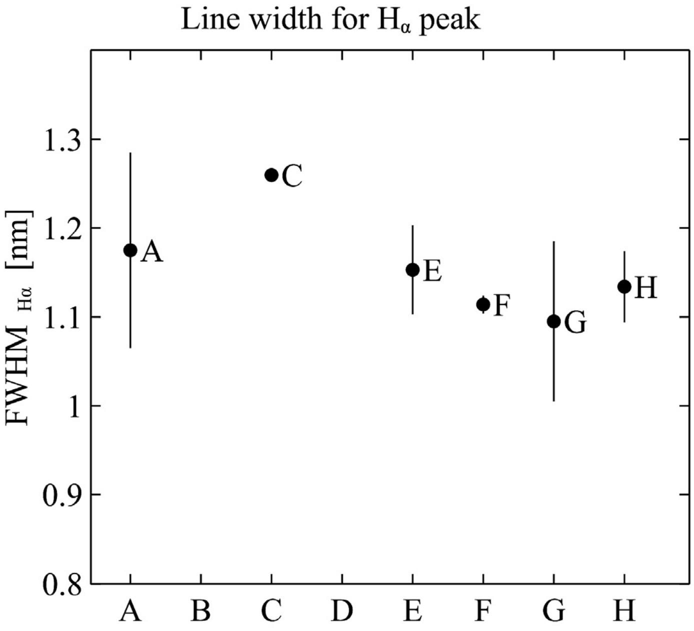

Figure 16- FWHM of H_α line at different deposition conditions.

Actinometry

Referring back to the Materials and Methods section, the relative intensity of CH, H_α and H_β, with respect to that of Ar ($4p \rightarrow 4s$ at 750nm) [36,74] at different plasma conditions, are employed as an index of concentration for CH and atomic hydrogen, respectively. Details on the concentration measurement of plasma species based on their intensity in OES spectra are provided in Chapter 3. Figure 17 shows calculated values of relative spectral lines intensity for different plasma species that could be used as an index for their concentrations during a deposition process. The I_{CH}/I_H ratio is also included in the graph, as it has been previously employed by Ebihara and Pastol to measure CH/H concentration in a plasma medium [36,68].

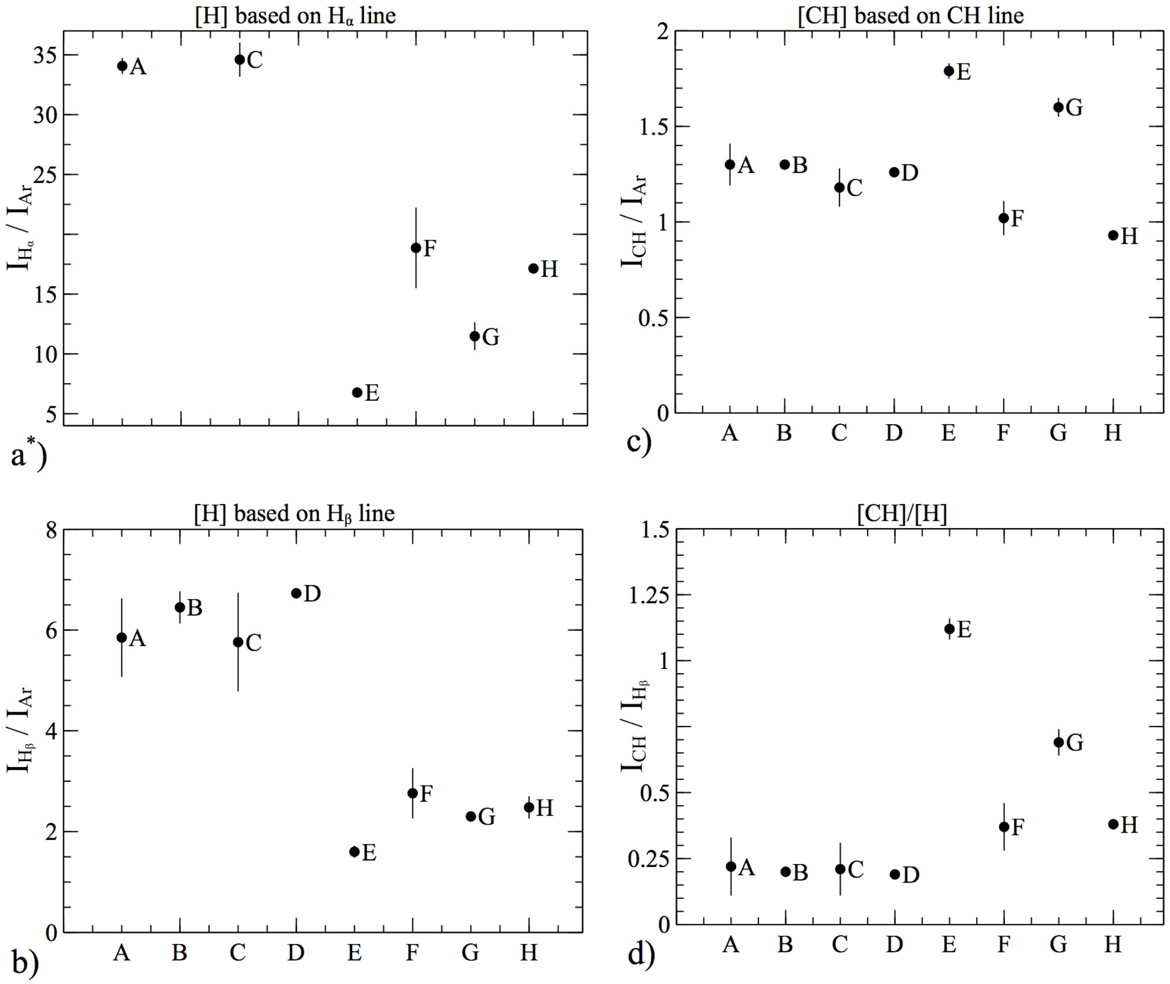

Figure 17- The intensity ratios as a probe of each species concentration in the plasma medium for CH, H_α, and H_β. The relative ratio of [CH]/[H_β] is also presented.

*B and D observations are not present in this graph due to spectrometer detector saturation in these plasma conditions.

The effect of plasma power and mode are clearly reflected in actinometry results of hydrogen (Figure 17-a and b). The high power observations (A, B, C, and D) are completely separated from the low power observations (E, F, G, and H).

One may also notice the effect of plasma pressure that is more evident in the low power group of observations of the CH related graph (A, C, F, and H in Figure 17-c). High pressure results in lower concentrations of CH that can be due to lower electron energy at higher plasma pressure, because of their shorter mean free path. In case of hydrogen, it is not easy to make a conclusion about the effect of pressure on [H], since the effect of the pressure and the plasma mode is confounded. This will be discussed later in section 4.5.3.

The effect of the plasma mode is evident in [H] (Figure 17-a and b). Higher concentrations of the atomic H are produced at the continuous mode of plasma power (B, D, F and H) where higher amounts of energy are delivered to the plasma species compared to the whole cycle of a pulse mode condition. Again, the effect of the plasma mode on [CH] is not clear from this graph since it is confounded with the pressure effect.

With these results, one can justify the reason that there is no coating in A and B deposition conditions. The CH_x deposition and hydrogen etching are both involved in a DLC coating growth in a competitive manner [100]. Greater population of the H atom in these two observations (as depicted in Figure 17–a and b), resulting from high plasma power, confirms the idea that the etching rate surpasses the deposition rate. Therefore, despite having large amounts of CH species (Figure 17-c), it is not possible to develop a stable amorphous carbon layer over the substrate.

The raw data, from these observations, are used as input information for the statistical analysis. The first step in this analysis is to study the effect of experimental parameters on OES data and to find how each OES data is related to each experimental parameter. After, both groups of data (experimental parameters and OES data) will be used as the input data to study their effect on DLC properties.

4.5.3 Effect of Experimental parameters on OES data

In this section a multivariate analysis method is used to study the effect of the process parameter on OES derived data.

A PLS model was developed based on the experimental parameters (plasma power, pressure and mode) and the OES data to study how the OES derived data change with experimental parameters. The bias voltage (V_b) is not considered in this model, since it is supposed to affect the plasma only in the vicinity of the substrate holder, while the recorded spectra are related to the bulk plasma that is far from the substrate holder. To verify this idea, the optical spectra of two groups of observations, with the same range of experimental parameters for plasma power, pressure and mode, but different bias voltage (V_b) values, were compared (Figure 18). As it is depicted the changes in V_b do not affect the spectra. Therefore, it is rational to exclude the V_b while one studies the effects of process parameters on OES data.

The loading bi-plot and the regression coefficients, resulted from PLSR studies, help to understand data structure and the correlation between the input and the output data. The loading plot of a PLSR analysis shows the data structure in each set of data and at the same time it describes how the variables in the Y matrix are correlated to the variables in the X matrix, based on first two principal components, while the regression coefficient plot considers all employed components (here A=3).

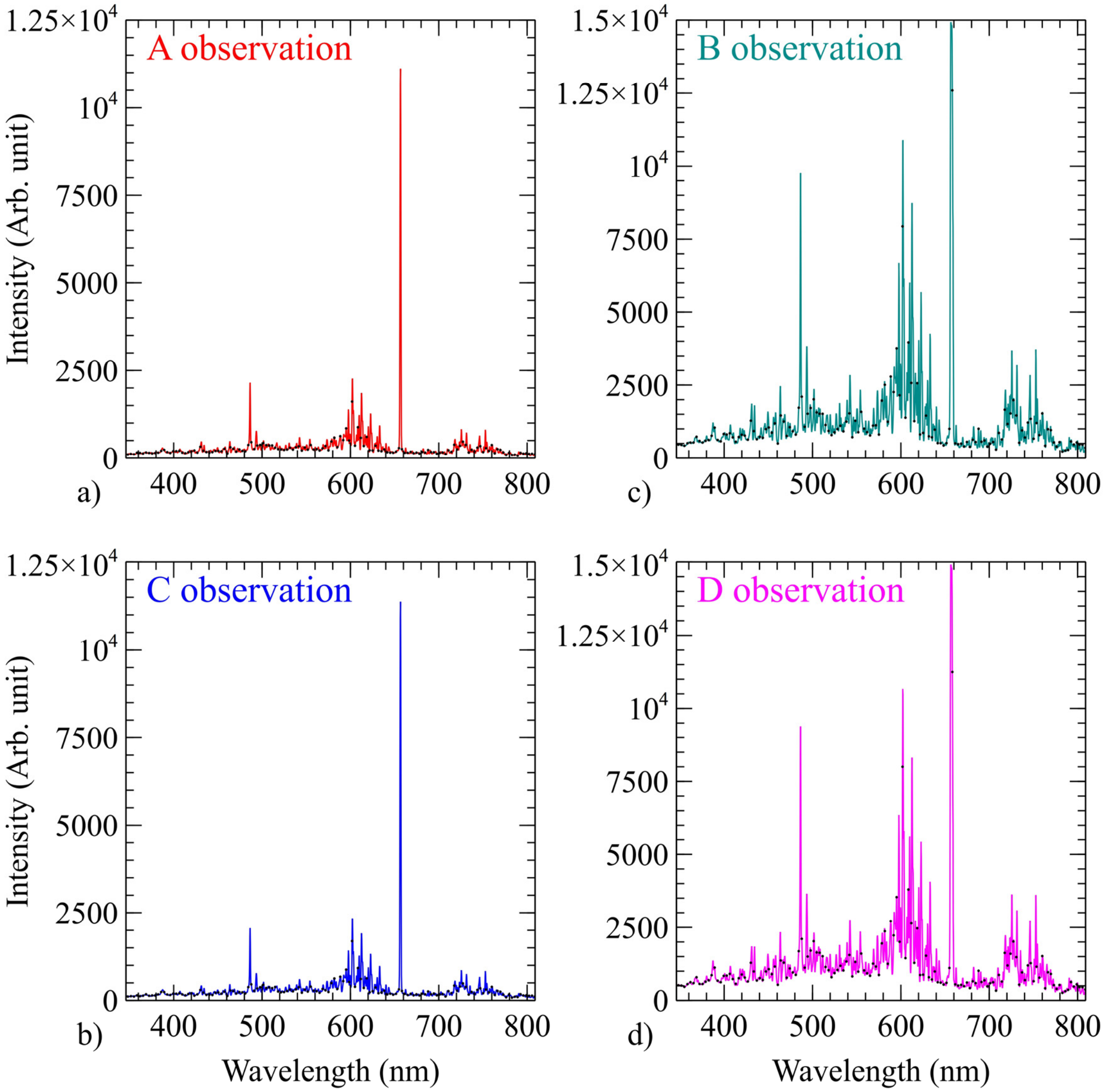

Figure 18- Example of OES results of two different bias voltage levels for two groups of observations; First, high power, high pressure, pulse mode, and high V_b for A observation and low V_b for C observation (a and b, respectively). Second, high power, low pressure, continuous mode, and high V_b for B observation and low V_b for D observation (c and d, respectively).

Figure 19 shows the loading plot of this PLSR model. The X and the Y-axis are the first and the second principal components. The distance between two parameters of the same data sets directly indicates how these two parameters are correlated. That is the reason that the three experimental parameters (P, p, and M) are located as far as possible from each other. This also indicates the importance of each parameter in the model, which is directly related to its distance from the plot origin (the closer the distance to the origin, the lower the importance for the model). Furthermore, X and Y parameters located in a same quadrant are directly correlated. Accordingly, it is evident that the I_H/I_{Ar} ratio is directly correlated to the plasma power (P), but inversely correlated with the plasma mode (M) and pressure (p). In the same way, the $FWHM_{H\alpha}$ shows a direct correlation to the plasma power and an inverse correlation to the plasma mode and pressure. The I_{CH}/I_{Ar} ratio, however, changes directly with the plasma mode but inversely with the plasma pressure and power.

The $FWHM_{H\beta}$ derived from H_β lines is located at the vicinity of the origin. This confirms the low importance of this parameter for the model. This supports the idea of not involving it in the analyses.

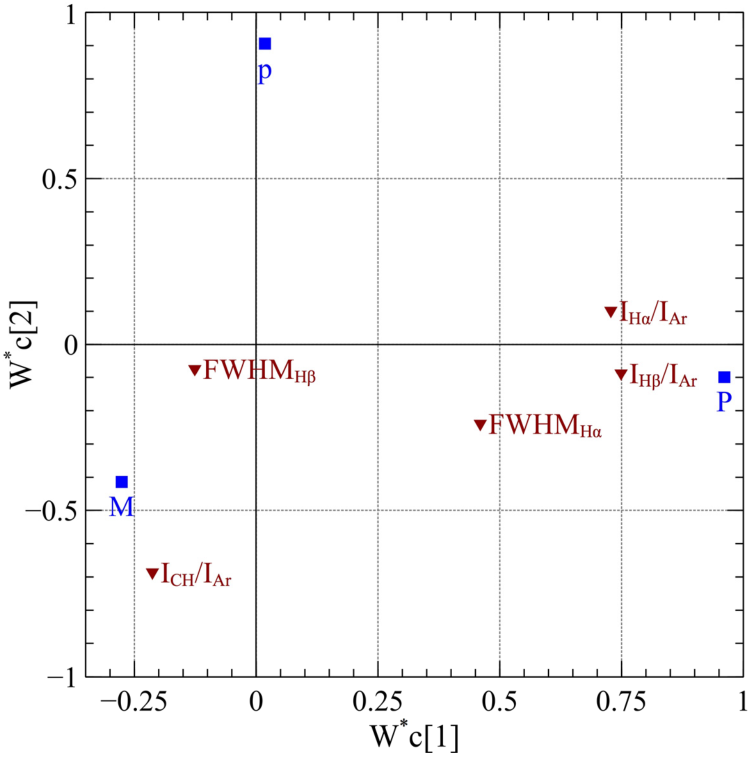

Figure 19- Loading bi-plot shows the relation between experimental parameters (P, p, and M) and the OES derived data.

The regression coefficients are presented in Figure 20. They show the effect of each single process parameter on each plasma characteristic.

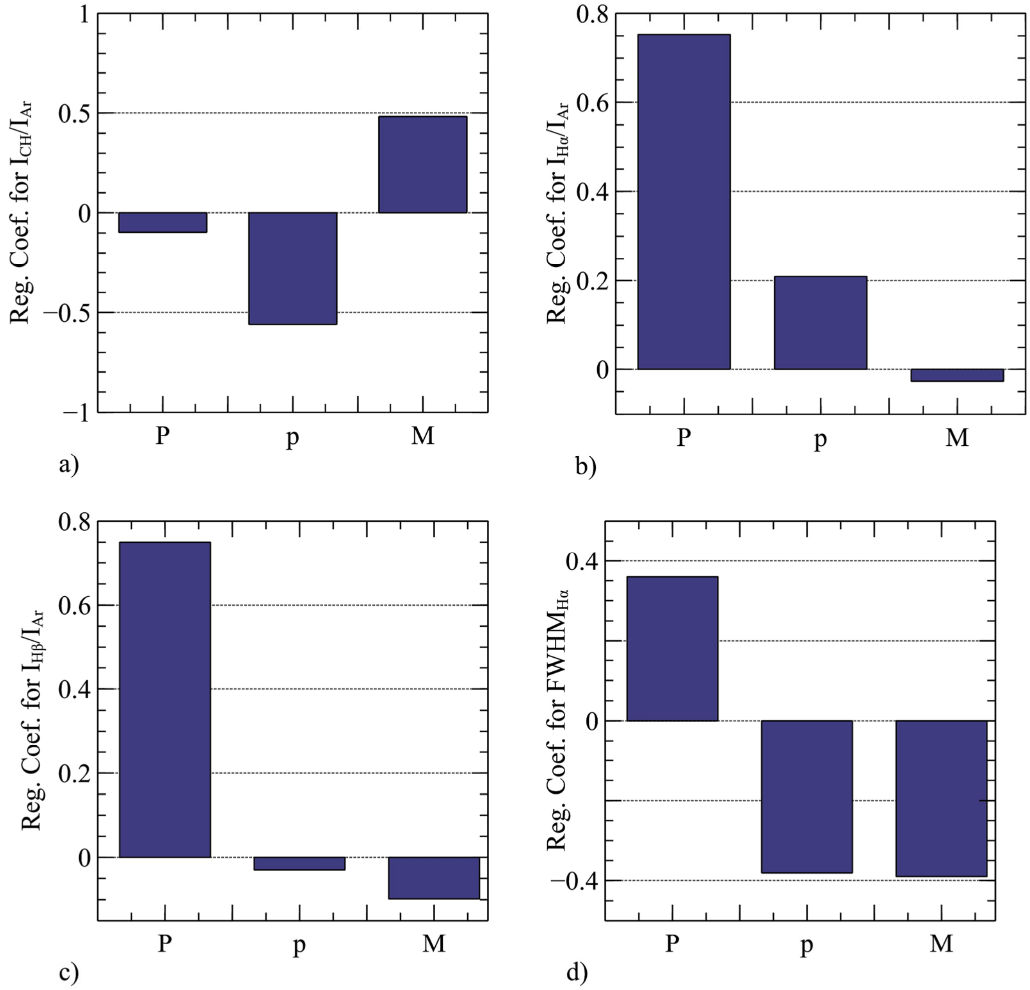

Figure 20- Regression coefficients of the PLSR model that show how the OES data change with experimental parameters.

Based on this graph, high concentration of atomic hydrogen is achieved at a high plasma power while the plasma mode and the plasma pressure have very small influences on it (Figure 20-b and c).

The effect of the plasma mode on CH concentration was not clear from raw data (Figure 17-c). However, the regression coefficients (Figure 20-a) show that it is directly affected by the plasma mode (M) and inversely by the plasma pressure (p). Therefore, the PLSR model helps to discover the confounded effect of the plasma mode and the pressure on CH concentration representative.

4.5.4 OES as a process-monitoring tool

The correlation between experimental parameters and/or OES data and DLC properties is discussed in this section. Four different PLSR models are developed in order to evaluate the OES potential in DLC coating property prediction, as presented in Table 16. Here, the DLC properties are used as the Y matrix in all the four models. The first model considers both the OES data and the experimental parameters as independent variables (X matrix). The second model employs just the experimental parameters as X to find out how a model without OES results can fit the data set. In the third model, the X matrix is just based on OES results. Finally, in the fourth model, the X matrix is built-up using the bias voltage and the OES data (Table 16).

Table 16- Components and the R^2 value of different PLSR models.

	Predictor Matrix		Predicted Matrix	R^2	$Q^{2`}$	A
1	P, M, p, V_b	OES	DLC properties	0.87	0.7	4
2	P, M, p, V_b	-	DLC properties	0.86	0.7	3
3	-	OES	DLC properties	0.60	0.2	4
4	V_b	OES	DLC properties	0.88	0.7	4

The R^2 value of a model shows how well each model fits its data space. Each new principal component increases the R^2 value, but not necessarily the prediction power of the model. Cross-Validation method is utilized to determine the number of principal components (A). Q^2 is the parameter that describes the effect of a new component in a model by evaluating how well it predicts the observations. A model is considered as a good explanation of the data space as long as $Q^2 \geq 0.5$ [105]. Details about R^2 and Q^2 are presented in the appendix B.

As expected, building-up the X matrix with all available input parameters (model 1) lead to the best predictive model with R^2 and Q^2 values of 0.87 and 0.7, respectively. Referring to Table 16, it is evident that removing the OES data from the model (model 2) does not lead to a significant decrease of its accuracy, since only a slight decrease of the R^2 value is observed. On the contrary, keeping only OES data (model 3) makes a prediction impossible, since both the R^2 and Q^2 values severely decrease. In these circumstances, this combination of OES data does not carry enough information about the process that can be used alone for DLC property prediction. As it is depicted in Figure 18, the OES spectra do not carry information from the bias voltage, which has a key role on DLC coating formation [14]. In these circumstances, a fourth model (model 4) was developed based on V_b and OES data as the predictor matrix. In this case, both the R^2 and the Q^2 values are almost identical to those of model 1. This means that it is possible to replace some of the plasma process parameters (power, duty cycle and pressure) by OES data without impeding the accuracy of the prediction on the DLC properties.

It is important to note that the fourth model, containing V_b and OES data, compares advantageously with the second model, made from just experimental parameters (including V_b). The fact that these two models lead to almost identical values of R^2 and Q^2 means that plasma experimental parameters can be replaced by OES data. In other words, the DLC layer characteristics can be followed in situ by simply monitoring V_b and recording OES spectra.

To find the most important variables that affect the process, one can study the Variable Importance Plots (VIPs) produced in a PLSR analysis. The VIP for models 2 and 4 are presented in Figure 21. The Parameters with a VIP value higher than unity are considered as very important, the values between 0.8 and 1 are considered as moderately important, while those less than 0.8 are not important in the modeling. In this way, the bias voltage (V_b) and the plasma power (P) are the most important parameters of model 2. It also shows that the atomic hydrogen and CH radical concentration (as measured by actinometry) have a key role to determine DLC properties. The low importance of $FWHM_{H\alpha}$ (used as a probe for gas temperature) on the DLC properties is probably related to the fact that the PECVD is a low temperature plasma process that is governed by electron impact dissociation rather than thermal dissociation[106].

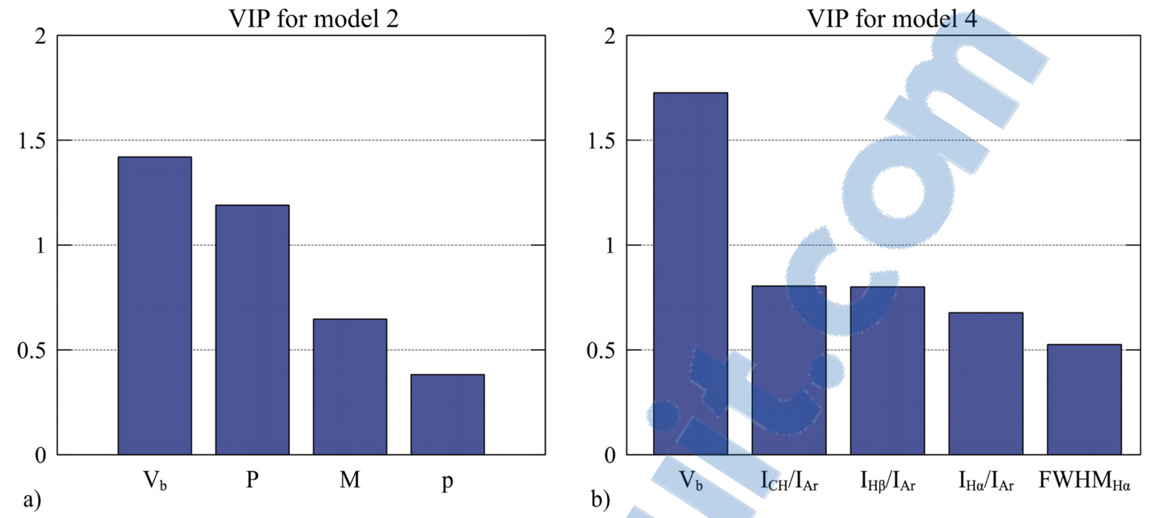

Figure 21- VIP bar plot of model 2 and 4. The parameters with a VIP value higher than 1 are very important in the model.

The VIP graph of model 4 introduces the bias voltage as the most important parameter. It is in agreement with the nature of DLC coating formation in which the energy of the incident ions, provided by applying a bias voltage, is responsible for sp^3/sp^2 ratio[14]. It is also interesting to note that the atomic hydrogen and CH radical concentrations drive the DLC properties. This latter mathematical observation finds its physical significance, because a DLC coating formation is an outcome of carbon deposition and hydrogen etching [100]. The H concentration can also affect the hydrogen content in the coating (the later needs to be evaluated by measuring DLC H-content).

To understand how DLC properties are affected by each parameter, one needs to study the regression coefficients and the loading plot of model 4. Figure 22 depicts the loading plot of model 4 based on the first two principal components. The regression coefficient plot considers all of the principal components (here A=4) and therefore, it is more precise than the loading plot. The coefficients related to the film stress, the D-parameter (D) and the deposition rate (r) that are derived from model 4, are presented in Figure 23. These two figures are used to explain DLC coating properties and structure based on using the deposition conditions and the plasma characteristics.

The film stress is directly correlated with bias voltage which means that the higher the voltage the higher the stress level in the coating. This can be explained by the fact that the bias voltage is responsible for ion acceleration toward the surface and higher energy ions create larger thermal spikes (as introduced by Bilek and McKenzi [29]). However, referring to Figure 7, one can conclude that the employed range of experimental parameters for DLC deposition fall to the left side of the graph (before the maximum), where the film stress level increases with the ion energy. It should be considered that the DLC deposited in this study is in the range of ta-C:H and a-C:H, and the presence of hydrogen in the structure reduces the stiffness of the DLC structure compared to that of diamond.

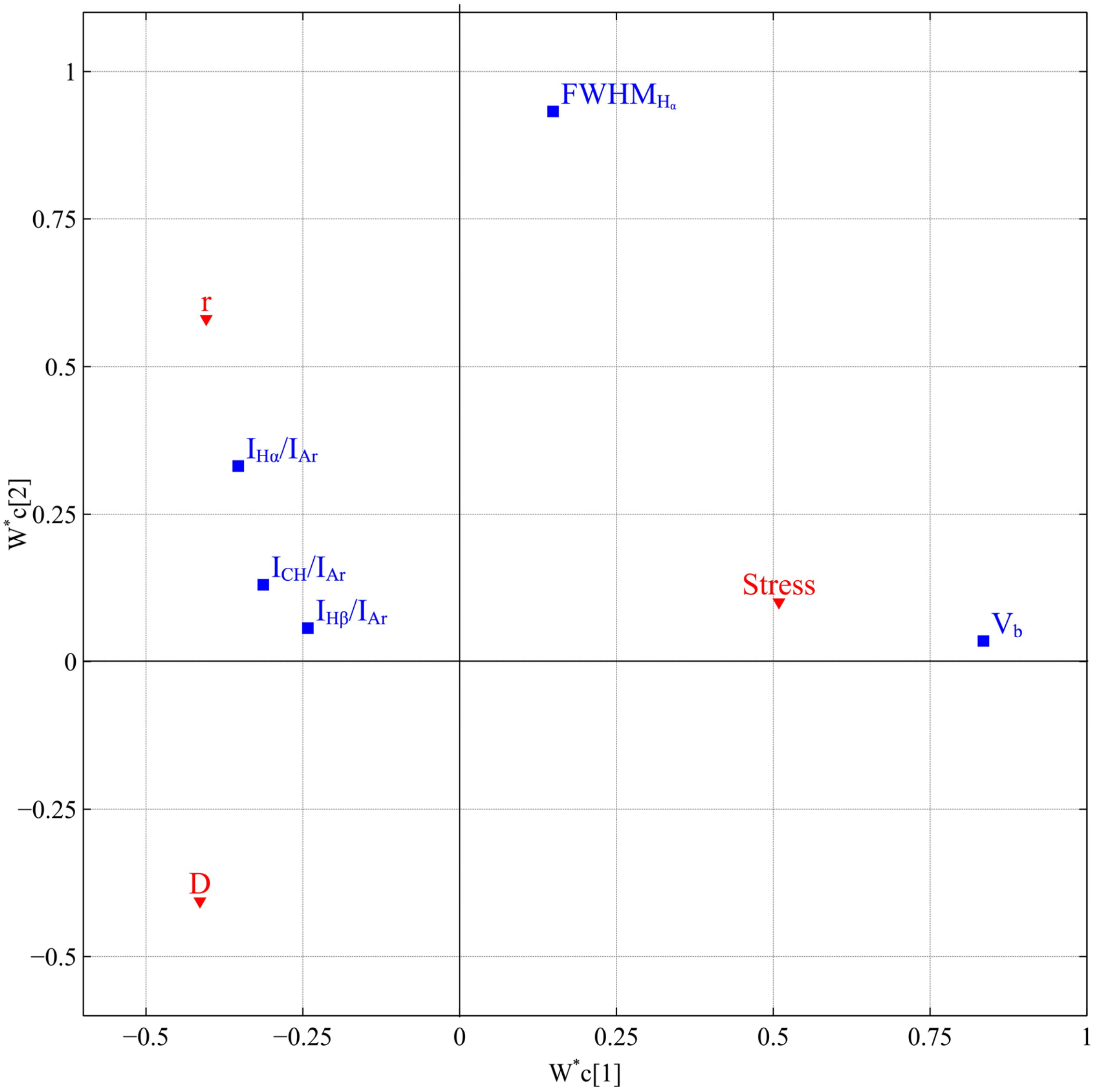

Figure 22- The loading plot of model 4 describes the correlation between DLC properties (red parameters) and input data (blue parameters).

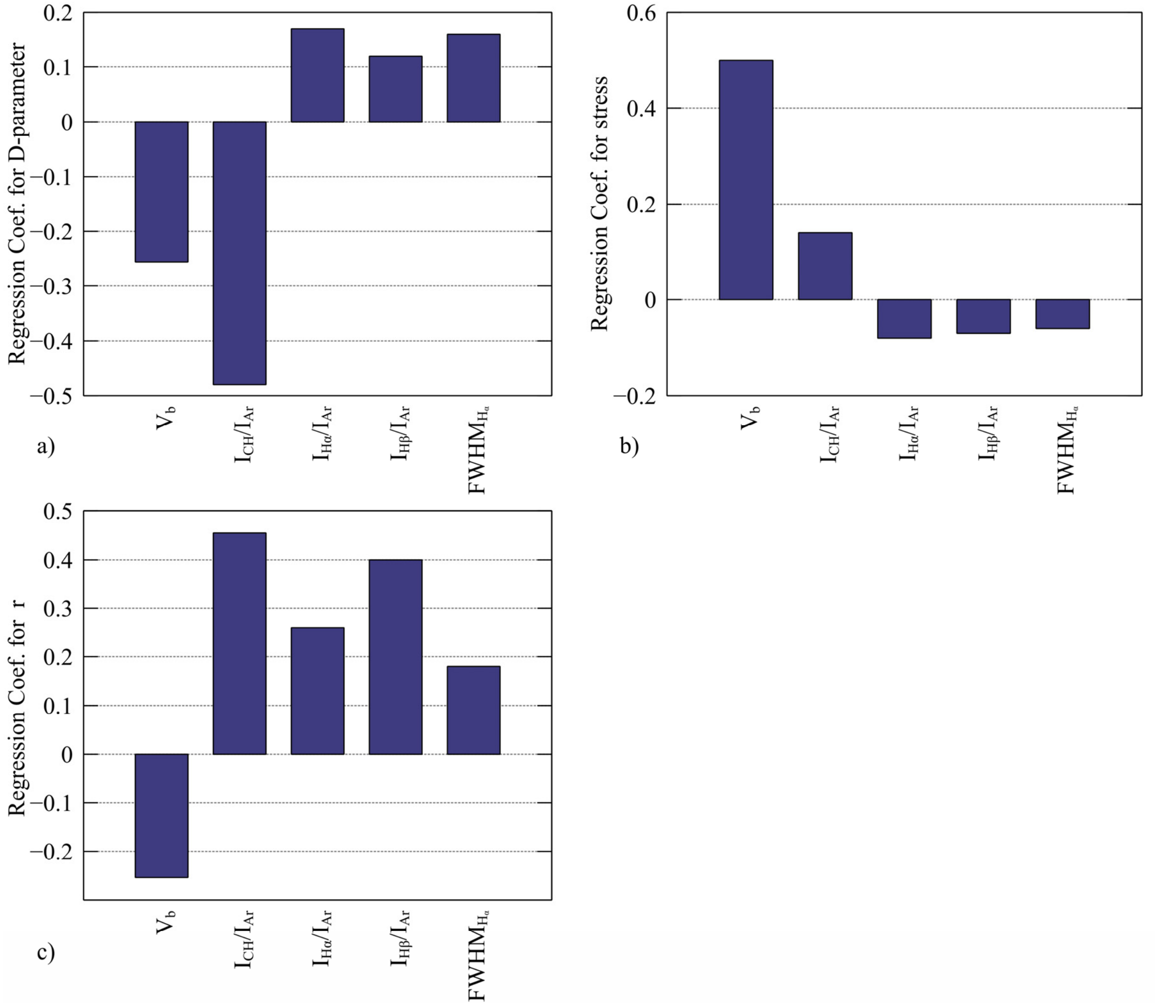

Figure 23- The regression coefficients for a) the D-parameter, b) the film stress, and c) the deposition rate of DLC coatings.

Figure 23-a shows that the D-parameter is inversely correlated with the bias voltage (V_b) and I_{CH}/I_{Ar}. Therefore, a lower D value is achieved at higher concentrations of CH and a larger bias voltage. According to regression coefficients, the most important parameter for the film stress is the bias voltage (Figure 23-b), which concurs with previous results on the effect of the bias voltage on the energy of incident ions and consequently on film stress [29]. This shows that D-parameter and film stress variation do not necessarily follow the same trend. In other words, it would be possible to deposit a DLC coating with a low D-parameter value (diamond like structure), but with a lower level of internal stress.

Atomic hydrogen concentration in plasma (I_H/I_{Ar}) is directly linked to the D-parameter. This means that higher atomic hydrogen concentration results in a more graphitic structure in the coating. An explanation is that when an atomic hydrogen touches the coating surface, there is a high probability that it will be bonded to another hydrogen atom from the coating surface and will form a H_2 molecule. This will produce a dangling bond on the coating surface that could be π-bonded to an adjacent carbon atom in a graphitic structure.

The DLC deposition rate decreases by increasing V_b likely because of a higher etching rate at a higher bias voltage. However, it increases with CH and atomic H concentration in plasma (Figure 23-c). Presence of hydrogen in a PECVD process facilitates DLC growth and therefore its deposition rate via different mechanisms. This takes place either in the plasma itself or at the plasma interface with a coating. It helps to break large molecules and prevent formation of aromatic species that could result in a non-diamond coating [107]. Creating active sites via breaking C=C bonds, removing soft graphitic or polymeric structures faster than diamond structure [108,109] and extracting H from C-H bonds by penetrating deep into the coating, are some of the hydrogen roles in DLC coating formation that could affect the DLC deposition rate (r).

To conclude the following results are derived from this discussion:

1. A PLSR model is a useful technique to study the DLC coating deposition process because it shows how each single coating properties is correlated with the independent parameters of the process.
2. The PLSR analysis also demonstrates the importance of the OES data in representing a part of process parameters (plasma power, mode, and pressure in this study).
3. The OES technique has the potential to be employed as a process-monitoring tool in the PECVD of DLC coatings.

Section 4.4.5 examines the power of model 4 in the prediction of new DLC coating properties.

4.5.5 Prediction of DLC properties using a PLSR model

To evaluate the prediction power of model 4, more experiments were carried out using a new combination of experimental parameters (as shown in Table 13). The three DLC parameters were then estimated based on the OES derived data and the applied bias voltage, using model 4. The three graphs in Figure 24 show observed and predicted values for each DLC parameter. Both the film stress and the D-parameter have a root-mean-squared error (RMSEP) value of less than one, which shows minimal errors in the prediction. The larger RMSEP for deposition rate can be related to the other variables that are not included in this model, such as substrate temperature, as proposed in other studies [14,18]. However, the prediction curve follows the trend of the observation in all three graphs, therefore confirming the PLSR model potential to predict DLC properties.

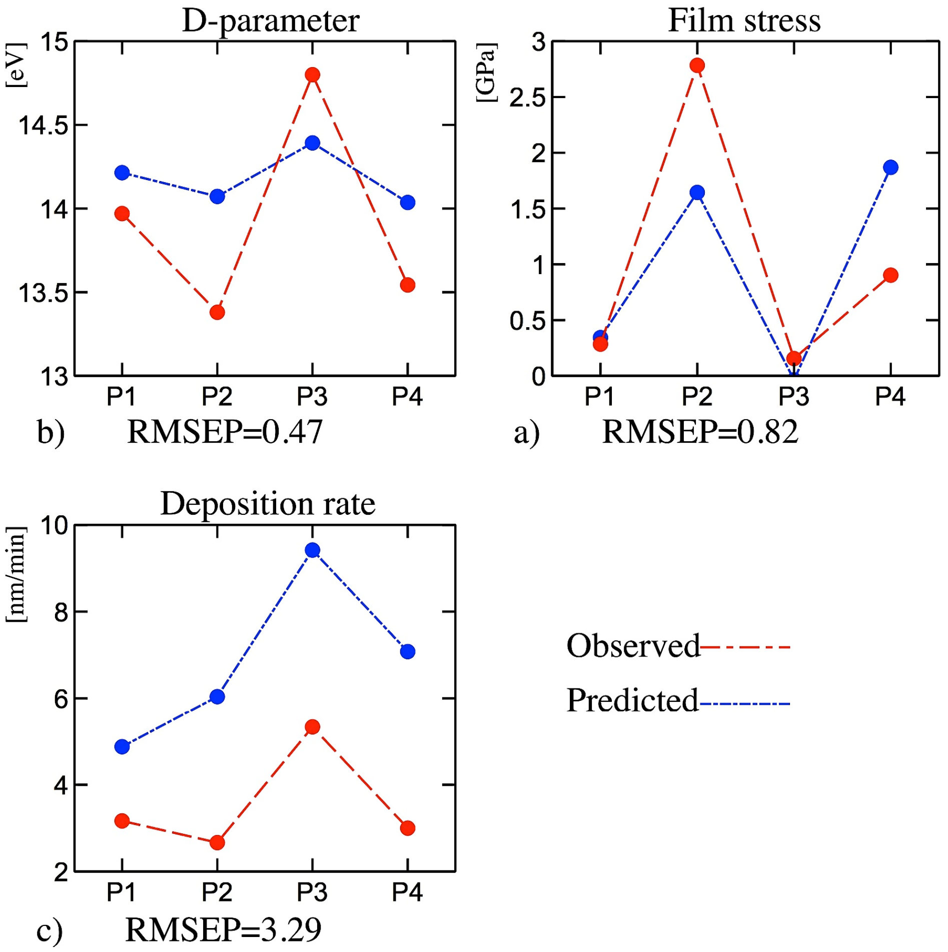

b) RMSEP=0.47

a) RMSEP=0.82

c) RMSEP=3.29

Figure 24- Predicted versus observed values for the DLC stress level, the D-parameter, and the deposition rate.

Based on these results, the model developed using the PLSR analysis has the potential to be employed for the coating property prediction (especially for the film stress and the D-parameter value). The prediction power can be improved by applying more parameters of the process into the model (such as the substrate temperature). For further development of the model, it would be interesting to incorporate other coating properties such as: hardness, optical properties, electrical properties, and other structural characteristics, according to specific applications of coatings.

4.5.6 Designing and monitoring a deposition process using the PLSR results

Finally, there are two other interesting applications of a PLSR analysis. The first is to design a deposition process. The second is to define a process window, based on the predictive power of the model, to achieve a desired property in the coating. The contour plots in Figure 25 (derived from model 2) show how the DLC film stress, the D-parameter value and the deposition rate (r) change with the main process parameters, which are the bias voltage (V_b) and the plasma power (P). It is not possible to find the optimum combination of process parameters to achieve a desired coating structure and properties. These graphs can also be used to design a gradient DLC structure to reduce the risk of coating delamination due to a high internal compressive stress.

A compromise between a low D value (diamond structure) and a medium stress level (lower risk of coating delamination) can be found from these contour plots. Based on these graphs, a diamond-like structure with a medium level of compressive stress can be achievable at a bias voltage range between 120-150 V and at a plasma power of around 100-150 W (Figure 25-a) (when we used our own plasma reactor).

Such a graph could also be employed to design a gradient DLC structure to reduce the risk of coating delamination due to a high internal compressive stress. In this way, an option is to start depositing a coating with a moderate stress and a medium D-parameter (Figure 25-a) and change it gradually toward a high stress and a low–D parameter coating (Figure 25-b), which also has more diamond like properties. Figure 25-c depicts the previous start- and end-point deposition windows that are superimposed to the deposition rate contour plot. It helps to choose a deposition system of a higher deposition rate.

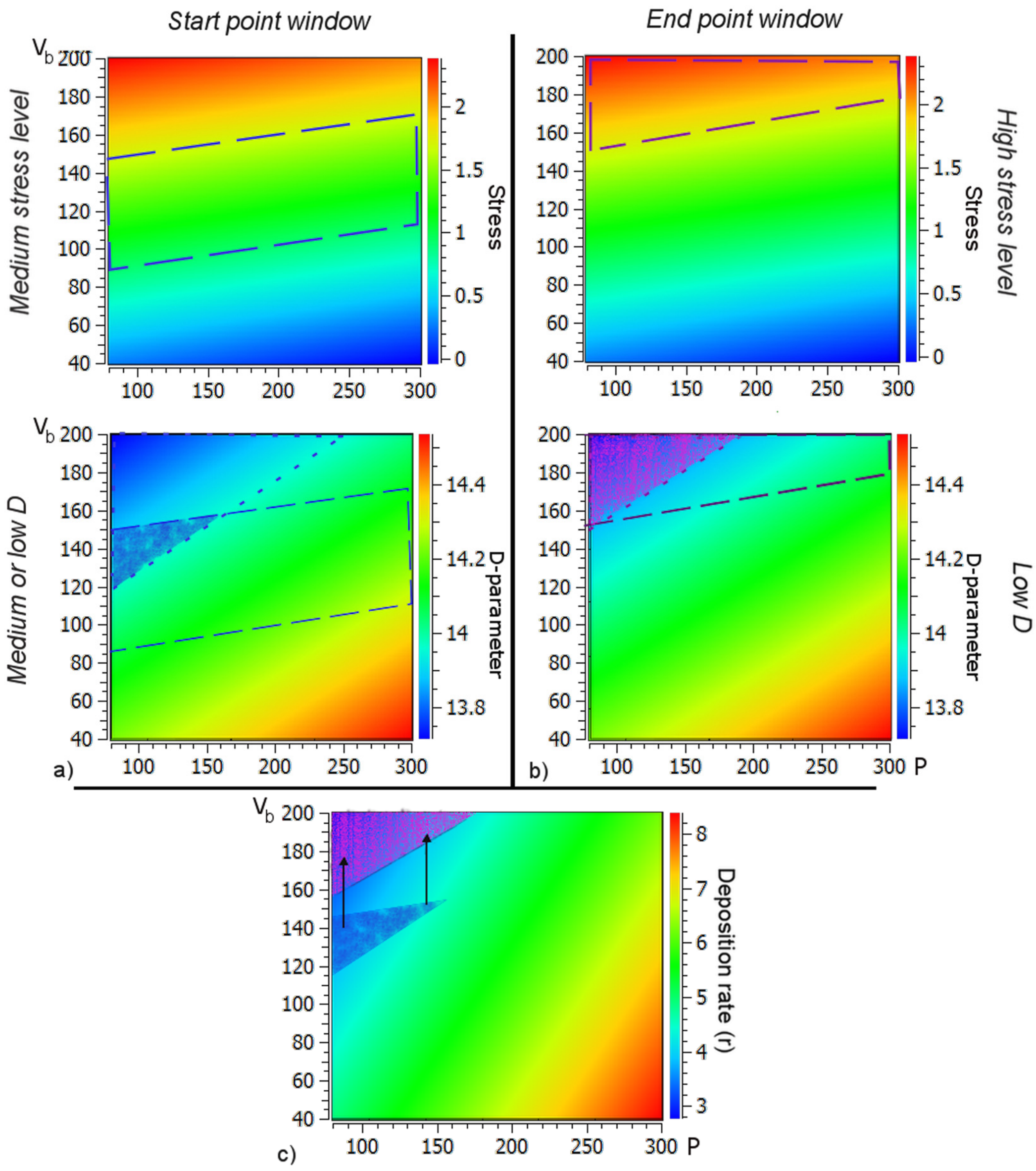

Figure 25- Designing a gradient DLC deposition using contour plots based on the bias voltage and the plasma power derived from model 2. Graph a) shows the starting window in which a medium stress and a medium D value are required. Graph b) shows the ending window in which a high stress and a low D value are required. Graph c) is the contour plot of the deposition rate including the starting and the ending window to select a deposition system with the desired deposition rate.

The same method, based on the most important variables among the OES data (I_{CH}/I_{Ar} and $I_{H\beta}/I_{Ar}$), can also be used to monitor the deposition process and to assure the desired properties in the growing layer of the DLC coating. The contour plots of the coating stress, the D-parameter, and the deposition rate as a function of the most important OES data, are presented in Figure 26. Similar to the designing step, two deposition regions are determined for the beginning and the end of a DLC deposition in order to achieve the same gradual structure (Figure 26-a and b). These monitoring regions are independent of the plasma reactor and its dependent process parameters, thus it could be used in any other PECVD system.

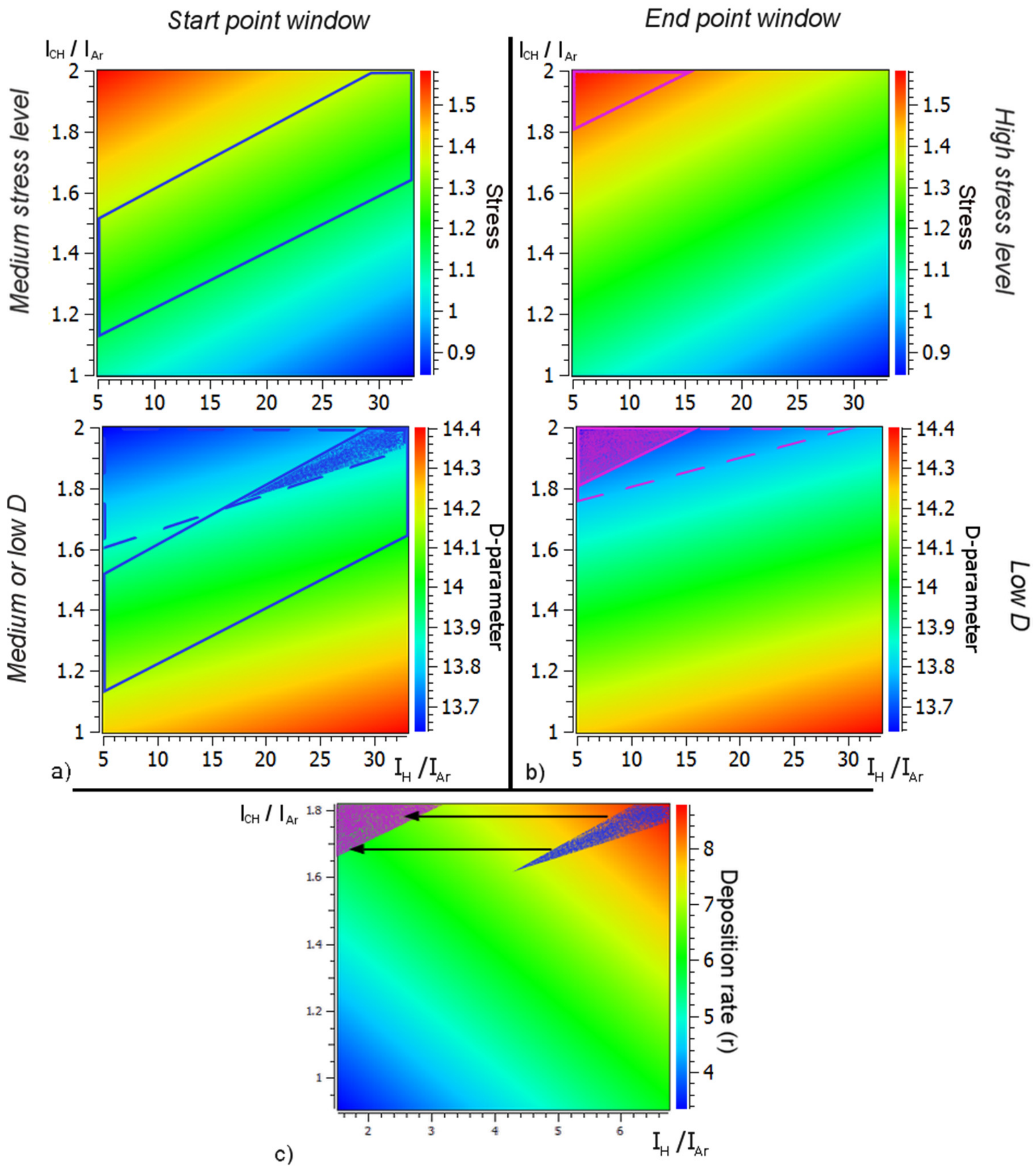

Figure 26- Monitoring a gradient DLC deposition using contour plots based on [H] and [CH] related parameters derived from model 4. Graph a) shows the starting window in which a medium stress and a medium D value are required. Graph b) shows the ending window in which a high stress and a low D value are required. Graph c) is the contour plot of the deposition rate with the starting and the ending window to select a deposition system with the desired deposition rate.

5 Conclusion

A statistical analysis was performed to compare two process control protocols for a PECVD of DLC coating. On one hand, the first protocol used plasma experimental parameters (the bias voltage, the plasma duty cycle, the plasma pressure, and the plasma power). On the other hand, the second process control was based on the parameters derived from the optical emission spectroscopy during the DLC deposition process. It was demonstrated that the bias voltage value had to be kept in any model aiming at controlling a DLC coating process. However, it was also found that all other aforementioned plasma parameters could be advantageously replaced by optical emission spectroscopy data. As a result, this allows reproducing the same DLC properties in any plasma reactor configuration and paves the way to use the OES as a monitoring tool for the DLC depositions, especially in a multilayer or gradient DLC coating deposition, where *in situ* coating properties have to be modified during the deposition process.

5.1 General conclusion

The following general conclusions are achieved based on the experiments in the specific range of experimental parameters of this study:

1- Optical emission spectroscopy as a process-monitoring tool is applicable in PECVD of a DLC coating.

2- OES has the potential to represent some of the experimental parameters. The plasma power, pressure, and mode have been replaced in this study.

3- The plasma power and the bias voltage are the two most effective parameters among the process parameters that determine the final DLC coating structure and properties.

5.2 Specific conclusion

The following conclusions are also achieved based on the experiments in the specific range of experimental parameters of this project:

1- In a combination of high plasma power and high bias voltage (conditions A and B), the etching rate surpass the deposition rate. Therefore, no stable coating will be produced.

2- The un-scratchable coatings took place at a high bias voltage and a low plasma power (conditions E and F) in which there were enough carbon species for high energetic incidents and therefore a high sp^3 coating formation.

3- Based on the PLSR results the H concentration and the CH concentration related variable, $I_{H\beta}/I_{Ar}$ and I_{CH}/I_{Ar}, respectively, were the two most important OES derived data.

4- The FWHM of H_α, which was a used as a probe for gas temperature (T_g), did not play an important role in such low-pressure plasma in which the plasma was mainly produced and controlled by electron impact excitations.

5.3 Suggestions for further study

There are some points to be considered in order to improve the model precision and prediction power. There are also several ideas and hypotheses that evolved during this study and can be a topic for future research. Among them, I would like to mention to the following suggestions:

1- To examine how OES can represent the effect of different gas precursors and different flow rates in a PECVD of a DLC.

In this study, methane, at a constant flow rate, was employed for all deposition conditions due to various technical restrictions. However, a variety of precursor gases with different flow rates can be used for DLC deposition. Therefore, it is important to consider this parameter for further research and to study how OES can represent these parameters in a model.

2- To represent the role of the bias voltage (V_b) in the model using a proper diagnostic technique.

The Faraday's Cup System could be used in this way. Our designed Faraday's cup (as described in Appendix C) needs to be restructured in order to avoid the interruptions induced by the bias voltage application.

Another option is the mass spectroscopy, which can provide more detailed information not only about the energy of the incident species, but also about their chemical nature. However, it is an expensive technique and difficult to apply.

3- To incorporate complementary coating characterization methods (either structural or physical and mechanical properties). These methods can help improve the model precision and to examine the relation between the process parameters and the coating structure. Following characterization can be employed:

- DLC coating H-content measurement.

There are different techniques that can be employed depending on the desired precision and resolution such as: Fourier Transform Infrared (FTIR) spectroscopy[1], Elastic Recoil Detection analysis (ERDA) [110,111], ERDA Time of Flight (ERDA-ToF) for profiling, and Nuclear Reaction Analysis (NRA) [24,112,113].

- The sp^3/sp^2 fraction measurement using Electron Energy Loss Spectroscopy or Nuclear Magnetic Resonance (NMR) [113].
- DLC coating density, mass, and thickness measurement using Rutherford Backscattering Spectroscopy (RBS)[111] or ellipsometry [114].
- Raman spectroscopy (UV range) to measure the sp^3/sp^2 ratio.
- Nano-indentation test to evaluate the hardness and Young's modulus of a DLC coating [115,116].

---

[1] According to Pie the fraction of optically active bonded hydrogen can be measured using FTIR [110].

References

1 A. Matthews and S. S. Eskildsen, *Diam. Relat. Mater.*, 1994, **3**, 902–911.

2 J. Robertson, *Phys. Status Solidi Appl. Mater. Sci.*, 2008, **205**, 2233–2244.

3 C. Casiraghi, J. Robertson and A. C. Ferrari, *Mater. Today*, 2007, **10**, 44–53.

4 R. Hauert, *Diam. Relat. Mater.*, 2003, **12**, 583–589.

5 F. R. Marciano, L. F. Bonetti, N. S. Da-Silva, E. J. Corat and V. J. Trava-Airoldi, *Appl. Surf. Sci.*, 2009, **255**, 8377–8382.

6 D. Batory, L. Kolodziejczyk and W. Szymanski, *Appl. Surf. Sci.*, 2013.

7 M. Ban and N. Hasegawa, *Diam. Relat. Mater.*, 2012, **25**, 92–97.

8 R. D. Boehm, C. Jin and R. J. Narayan, in *Comprehensive Biomaterials*, Elsevier, 2011, pp. 109–126.

9 J. C. Angus, Y. Wang and M. Sunkara, *Annu. Rev. Mater. Sci.*, 1991, **21**, 221–248.

10 Y. Lifshitz, *Diam. Relat. Mater.*, 1999, **8**, 1659–1676.

11 J. C. Angus, *Diam. Relat. Mater.*, 1991, **1**, 61–62.

12 J. Robertson, *Diam. Relat. Mater.*, 1994, **3**, 361–368.

13 W. Jacob and W. Möller, *Appl. Phys. Lett.*, 1993, **63**, 1771–1773.

14 J. Robertson, *Mater. Sci. Eng. R Reports*, 2002, **37**, 129–281.

15 M. Weiler, S. Sattel, K. Jung, H. Ehrhardt, V. S. Veerasamy and J. Robertson, *Appl. Phys. Lett.*, 1994, **64**, 2797–2799.

16 S. Aisenberg, *J. Appl. Phys.*, 1971, **42**, 2953.

17 B. P. B. Davies and P. M. Martineau, *Adv. Mater.*, 1992, **4**, 729–736.

18 Y. Lifshitz, *Diam. Relat. Mater.*, 1996, **5**, 388–400.

19 M. Meyyappan, *J. Phys. D. Appl. Phys.*, 2009, **42**, 213001.

20 G. H. Döhler, R. Dandoloff and H. Bilz, *J. Non. Cryst. Solids*, 1980, **42**, 87–95.

21 J. C. Angus, *J. Vac. Sci. Technol. A Vacuum, Surfaces, Film.*, 1988, **6**, 1778.

22 A. Von Keudell and W. Jacob, *J. Appl. Phys.*, 1996, **79**, 1092.

23 and J. W. R. Y. Lifshitz, S. R. Kasi, *Phys. Rev. Lett.*, 1989, **62**, 1290–1293.

24 J. Robertson, *Surf. Coatings Technol.*, 1992, **50**, 185–203.

25 C. Weissmantel, K. Bewilogua, K. Breuer, D. Dietrich, U. Ebersbach, H.-J. Erler, B. Rau and G. Reisse, *Thin Solid Films*, 1982, **96**, 31–44.

26 Y. Lifshitz, S. R. Kasi, J. W. Rabalais and W. Eckstein, *Phys. Rev. B*, 1989, **41**, 10468–10480.

27 D. R. McKenzie, D. Muller, B. A. Pailthorpe, Z. H. Wang, E. Kravtchinskaia, D. Segal, P. B. Lukins, P. D. Swift, P. J. Martin, G. Amaratunga, P. H. Gaskell and A. Saeed, *Diam. Relat. Mater.*, 1991, **1**, 51–59.

28 C. a. Davis, *Thin Solid Films*, 1993, **226**, 30–34.

29 M. M. M. Bilek and D. R. McKenzie, *Surf. Coatings Technol.*, 2006, **200**, 4345–4354.

30 N. Marks, *Phys. Rev. B*, 1997, **56**, 2441–2446.

31 S. M. Rossnagel, J. J. Cuomo and W. D. Westwood, 1990.

32 R. Rompe and M. Steenbeck, *Progress in plasmas and gas electronics*, Akademie-Verlag, 1975.

33 C. Corbella, M. Vives, G. Oncins, C. Canal, J. L. Andújar and E. Bertran, *Diam. Relat. Mater.*, 2004, **13**, 1494–1499.

34 V. A. Godyak, in *Plasma-Surface Interactions and Processing of Materials*, Springer Netherlands, 1990, pp. 95–134.

35 J. R. Woodworth, M. E. Riley, D. C. Meister, B. P. Aragon, M. S. Le and H. H. Sawin, *J. Appl. Phys.*, 1996, **80**, 1304.

36 A. Pastol and Y. Catherine, *J. Phys. D*, 1990, **23**, 799–805.

37 V. Schulz-von Der Gathen, *Plasma Sources Sci. Technol.*, 2001, **10**, 530.

38 G. Lombardi, K. Hassouni, F. Bénédic, F. Mohasseb, J. Röpcke and A. Gicquel, *J. Appl. Phys.*, 2004, **96**, 6739.

39 S. Naito, H. Nomura and T. Goto, *LASER Eng.*, 1992, 746.

40 N. Mutsukura, *Plasma Chem. Plasma Process.*, 2001, **21**, 265–277.

41 a. Soum-Glaude, L. Thomas, A. Dollet, P. Ségur and M. C. Bordage, *Diam. Relat. Mater.*, 2007, **16**, 1259–1263.

42 H. Zhou, J. Watanabe, M. Miyake, A. Ogino, M. Nagatsu and R. Zhan, *Diam. Relat. Mater.*, 2007, **16**, 675–678.

43 I. H. Hutchinson, *Principles of Plasma Diagnostics*, Cambridge Universty;, second., 2002.

44 M. Mavadat, A. Ricard, C. Sarra-Bournet and G. Laroche, *J. Phys. D. Appl. Phys.*, 2011, **44**, 155207.

45 J. Felts, *J. Vac. Sci. Technol. A Vacuum, Surfaces, Film.*, 1987, **5**, 2273.

46 V. A. Godyak, *PROBE DIAGNOSTICS OF RF PLASMAS FOR MATERIAL PROCESSING*, 2013.

47 B. E. Cherrington, *Plasma Chem. Plasma Process.*, 1982, **2**, 113–140.

48 M. Chhowalla, C. a Davis, M. Weiler, B. Kleinsorge and G. a J. Amaratunga, *J. Appl. Phys.*, 1996, **79**, 2237–2244.

49 M. M. M. Bilek, M. Chhowalla, M. Weiler and W. I. Milne, *J. Appl. Phys.*, 1996, **79**, 1287.

50 C. Wild and P. Koidl, *J. Appl. Phys.*, 1991, **69**, 2909–2922.

51 J. Wagner, C. Wild, F. Pohl and P. Koidl, *Appl. Phys. Lett.*, 1986, **48**, 106.

52 B. a. Cruden and M. Meyyappan, *J. Appl. Phys.*, 2005, **97**, 84311.

53 P. B. Davies and P. M. Martineau, *J. Appl. Phys.*, 1992, **71**, 6125.

54 C. Barholm-Hansen, M. D. Bentzon, M. E. Vigild, E. Findeise, R. Feidenhans and J. Bindslev, *Surf. Coatings Technol.*, 1994, **69**, 702–707.

55 K. J. Clay, S. P. Speakman, G. a. J. Amaratunga and S. R. P. Silva, *J. Appl. Phys.*, 1996, **79**, 7227–7233.

56 W. Y. Fan, P. F. Knewstubb, M. Ka, L. Mechold, J. Ro and P. B. Davies, *J. Phys. Chem. A*, 1999, **103**, 4118–4128.

57 C. Hollenstein, *Plasmas Polym.*, 1998, **3**, 249–256.

58 J. Wormhoudt and K. E. Mccurdy, *Chem. Phys. Lett.*, 1989, **156**, 47–50.

59 C. Wild, *J. Vac. Sci. Technol. A Vacuum, Surfaces, Film.*, 1987, **5**, 2227.

60 I. B. Denysenko, *J. Appl. Phys.*, 2004, **95**, 2713.

61 C. Cavallotti, M. Di Stanislao and S. Carrà, *Prog. Cryst. Growth Charact. Mater.*, 2004, **48–49**, 123–165.

62 H. Chu, E. Den Hartog, A. Lefkow, J. Jacobs, L. Anderson, M. Lagally and J. Lawler, *Phys. Rev. A*, 1991, **44**, 3796–3803.

63 V. M. Polushkin, a. T. Rakhimov, V. a. Samorodov, N. V. Suetin and M. a. Timofeyev, *Diam. Relat. Mater.*, 1994, **3**, 1385–1388.

64 G. Zambrano, H. Riascos, P. Prieto, E. Restrepo, A. Devia and C. Rincón, *Surf. Coatings Technol.*, 2003, **172**, 144–149.

65 S. Pellerin, K. Musiol, O. Motret, B. Pokrzywka and J. Chapelle, *J. Phys. D. Appl. Phys.*, 1996, **29**, 2850–2865.

66 D. M. Gruen, *J. Vac. Sci. Technol. A Vacuum, Surfaces, Film.*, 1995, **13**, 1628.

67 Nemes and Laszlo, *SPECTROSCOPY, DYNAMICS AND MOLECULAR THEORY OF CARBON PLASMAS AND VAPORS: ADVANCES IN THE UNDERSTANDING OF THE MOST COMPLEX HIGH-TEMPERATURE ELEMENTAL SYSTEM*, World Scientific Publishing Company, 2011.

68 K. Ebihara, T. Ikegami, T. Matsumoto, H. Nishimoto, S. Maeda and K. Harada, *J. Appl. Phys.*, 1989, **66**, 4996.

69 A. Gicquel, K. Hassouni, S. Farhat, Y. Breton, C. D. Scott, M. Lefebvre and M.

Pealat, *Diam. Relat. Mater.*, 1994, **3**, 581–586.

70 A. Gicquel, K. Hassouni, Y. Breton, M. Chenevier and J. C. Cubertafon, *Diam. Relat. Mater.*, 1996, **5**, 366–372.

71 M. H. Elghazaly, A. M. Abd Elbaky, A. H. Bassyouni and H. Tuczek, *J. Quant. Spectrosc. Radiat. Transf.*, 1999, **61**, 503–507.

72 T. Lang, J. Stiegler, Y. von Kaenel and E. Blank, *Diam. Relat. Mater.*, 1996, **5**, 1171–1184.

73 J. W. Coburn and M. Chen, *J. Appl. Phys.*, 1980, **51**, 3134.

74 A. Gicquel, M. Chenevier, K. Hassouni, A. Tserepi and M. Dubus, *J. Appl. Phys.*, 1998, **83**, 7504.

75 T. A. Friedmann, J. P. Sullivan, J. A. Knapp, D. R. Tallant, D. M. Follstaedt, D. L. Medlin and P. B. Mirkarimi, *Appl. Phys. Lett.*, 1997, **71**, 3820.

76 S. Takabayashi, K. Okamoto, H. Sakaue, T. Takahagi, K. Shimada and T. Nakatani, *J. Appl. Phys.*, 2008, **104**, 43512.

77 H. W. Choi, J.-H. Choi, K.-R. Lee, J.-P. Ahn and K. H. Oh, *Thin Solid Films*, 2007, **516**, 248–251.

78 J. L. Endrino, R. Escobar Galindo, H.-S. Zhang, M. Allen, R. Gago, A. Espinosa and A. Anders, *Surf. Coatings Technol.*, 2008, **202**, 3675–3682.

79 N. M. Chekan, N. M. Beliauski, V. V. Akulich, L. V. Pozdniak, E. K. Sergeeva, A. N. Chernov, V. V. Kazbanov and V. a. Kulchitsky, *Diam. Relat. Mater.*, 2009, **18**, 1006–1009.

80 J. Meneve, E. Dekempeneer, W. Wegener and J. Smeets, *Surf. Coatings Technol.*, 1996, **86–87**, 617–621.

81 S. Logothetidis, C. A. Charitidis, M. Gioti and Y. Panayiotatos, *Diam. Relat. Mater.*, 2000, **9**, 756–760.

82 Z. Xu, Y. J. Zheng, F. Jiang, Y. X. Leng, H. Sun and N. Huang, *Appl. Surf. Sci.*, 2013, **264**, 207–212.

83 Y. Pauleau and F. Thièry, *Surf. Coatings Technol.*, 2004, **180–181**, 313–322.

84 G. . Yin, J. . Luo, C. . Zheng, H. . Tong, Y. . Huo and L. . Mu, *Thin Solid Films*, 1999, **345**, 67–70.

85 J. Deng and M. Braun, *Diam. Relat. Mater.*, 1995, **9635**, 0–7.

86 A. A. Voevodin, C. Rebholz and A. Matthews, *Tribol. Int.*, 1996, **29**, 559–570.

87 C. Donnet and A. Erdemir, Eds., *Tribology of Diamond-Like Carbon Films*, Springer, New York : Springer, 2008.

88 R. J. Narayan, *J. Adhes. Sci. Technol.*, 2004, **18**, 1339–1365.

89 Y. F. Zheng, X. L. Liu and H. F. Zhang, *Surf. Coatings Technol.*, 2008, **202**, 3011–

3016.

90 T. M. Chao and A. H. Tan, *Mater. Des.*, 2013, **48**, 58–67.

91 H. Ronkainen, J. Koskinen, S. Varjus and K. Holmberg, *Surf. Coatings Technol.*, 1999, **122**, 150–160.

92 G. E. P. Box, S. Hunter, J and W. G. Hunter, *Statistics for experimenters, Design, Innovation and Discovery*, Wiley interscience, 2nd edn., 2005.

93 Y. Lifshitz, *Diam. Relat. Mater.*, 2003, **12**, 130–140.

94 G. G. Stoney, *Proc. R. Soc. London. Ser. A, Contain. Pap. a Math. Phys. Character*, 1909, **82**, 172–175.

95 A. A. Galuska and H. H. Madden, *Appl. Surf. Sci.*, 1988, **32**, 253–272.

96 T. Sharda, *J. Vac. Sci. Technol. A Vacuum, Surfaces, Film.*, 1998, **16**, 413.

97 Y. Mizokawa, T. Miyasato and K. M. Geib, *Surf. Sci.*, 1987, **182**, 431–438.

98 J. C. Lascovitch, R. Giorgi and S. Scaglione, *Appl. Surf. Sci.*, 1991, **47**, 17–21.

99 S. Wold and M. Sjostrom, *Chemom. Intell. Lab. Syst.*, 2001, **58**, 109–130.

100 A. Poukhovoi and S. Schipporeit, *J. Optoelectron. Adv. Mater.*, 2012, **14**, 383–392.

101 K. Teii, *J. Vac. Sci. Technol. A Vacuum, Surfaces, Film.*, 1999, **17**, 138.

102 K. W. Hemawan and R. J. Hemley, *J. Vac. Sci. Technol. A Vacuum, Surfaces, Film.*, 2015, **33**, 61302.

103 W. L. Wiese and J. R. Fuhr, *J. Phys. Chem. Ref. Data*, 2009, **38**, 565.

104 R. K. Garg, T. N. Anderson, R. P. Lucht, T. S. Fisher and J. P. Gore, *J. Phys. D. Appl. Phys.*, 2008, **41**, 95206.

105 M. C. N.-Q. A. 278. . T. 1998 Tenenhaus, *La régression PLS : théorie et pratique*, Éd. Technip, Paris, 1998.

106 A. A. Fridman and L. A. C. N.-Q. C. 718 F. 2011 Kennedy, *Plasma physics and engineering*, CRC Press, Boca Raton, FL, 2nd ed., 2011.

107 M. Frenklach, *J. Appl. Phys.*, 1989, **65**, 5142.

108 L. Schäfer, C.-P. Klages, U. Meier and K. Kohse-Höinghaus, *Appl. Phys. Lett.*, 1991, **58**, 571.

109 N. Setaka, *J. Mater. Res.*, 1989, **4**, 664–670.

110 Y. T. Pei, N. G. Chechenin, P. N. Chernykh, a. a. Turkin, D. Vainshtein and J. T. M. De Hosson, *Scr. Mater.*, 2009, **61**, 320–323.

111 J. W. Zou, K. Reichelt, K. Schmidt and B. Dischler, *J. Appl. Phys.*, 1989, **65**, 3914.

112 P. Koidl, *Mater. Sci. Forum*, 1991, **52**.

113 P. K. Chu and L. Li, *Mater. Chem. Phys.*, 2006, **96**, 253–277.

114 S. Logothetidis, S. Kassavetis, C. Charitidis, Y. Panayiotatos and A. Laskarakis, *Carbon N. Y.*, 2004, **42**, 1133–1136.

115 W. C. Oliver and G. M. Pharr, *J. Mater. Res.*, 2004, **19**, 3–20.

116 W. C. Oliver and G. M. Pharr, *J. Mater. Res.*, 1992, **7**.

117 K. Dunn, *Process Improvement using Data*, http://learnche.org/pid - Portions of this work are the copyright of ConnectMV, 2012.

118 R. H. Huddlestone and S. L. Leonard, *Plasma Diagnostic Techniques*, Academic Press Inc., 1965.

119 V. a Godyak and V. I. Demidov, *J. Phys. D. Appl. Phys.*, 2011, **44**, 269501.

120 N. J. Behlman, Wocester Polytechnic Institute, 2009.

Appendix

A. Auger Electron Spectroscopy (AES)

In this study the structural features of DLC were examined using a X-ray excited Auger electron spectroscopy (XAES) method.

X-ray photoelectron spectroscopy studies a material surface by measuring the kinetic energy of incoming photoelectrons, which are the product of the X-ray-surface interaction. The bonding energy of each carbon electrons varies with respect to the type of its chemical bonding therefor photoelectrons from carbons of different bonding conditions arrive to the XPS detector at different values of kinetic energy. So one can characterize not only different elements of the surface, but also their chemical state and the type of chemical bonds that they are involved in. The C1s peak of carbon is frequently used to detect carbon atoms with different chemical bonds. It is erroneous to distinguish between sp^2 and sp^3 hybridized carbon just based on C1s position. However, there are various studies on the application of XPS results for different carbon hybridization determination (Merel 1998).

A complementary technique for hybridization determination is Auger Electron Spectroscopy (AES). It is based on the analysis of the Auger electron energy level. The Auger effect happens when an electron of an outer-shell of an atom transfers to fill an inner-shell vacancy. The energy difference between the two states will be released in the form of electromagnetic waves and will eject a secondary electron from the outer shells. This electron is called Auger electron. The kinetic energy of Auger electrons is a characteristic of a material. The C KLL peak in AES spectrum (bonding energy range of 1200-1250 eV) is usually used for determination of carbon hybridization type. In 1987 Mizokawa et al. showed that the firs derivative of this peak (dN(E)/dE) can be used as an indicator of carbon fine structure [97]. The D-parameter in the first derivative of AES C KLL spectra, which is the distance between the lowest valley and the highest peak, could be an index of the sp^3 content. Graphite is characterized by a large D-parameter value (24 eV) while, diamond has a low D-parameter (14 eV) (Figure 27) [97,98]. The sp^3 fraction of a DLC film then can be calculated from its D-parameter.

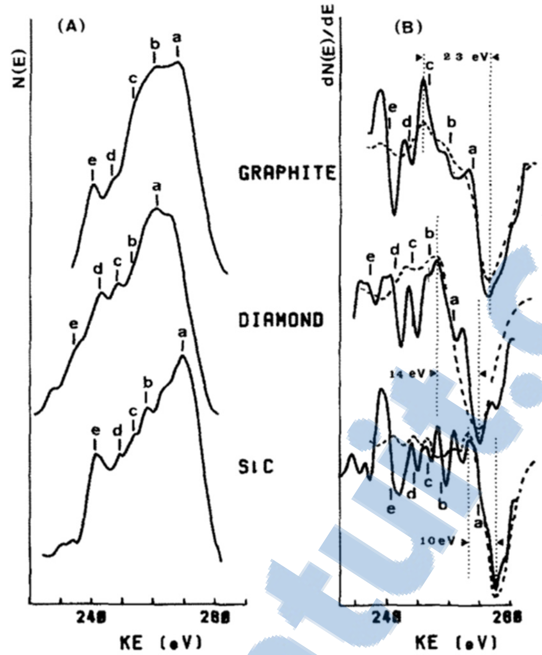

Figure 27- C KLL and the first derivative Auger spectra of graphite, diamond and SiC.

B. Partial Least Square Regression

A Multi Linear Regression (MLR) is a statistical method that widely used to correlate a set of independent variables with the resulted dependent parameters. However, the MLR is true when the X variables are few and un-correlated. While, usually several correlated variables are produced using new characterization techniques such as spectroscopy methods. In Partial Least Square Regression (PLSR), a set of orthogonal components, called *latent variables* (LV) (or principal components (PC)), which have the best predictive power, will be extracted from the X matrix. In other words, PLSR finds the best axes that simultaneously explain variations in X and predict Y. Comparing with traditional regression models, the PLSR analysis demonstrates the structure of both X and Y matrices. Moreover, it is able to examine data spaces with strongly collinear and noisy data, with numerous variables [99].

Principal Component Analysis (PCA)

The concept of a PLSR is similar to that of a Principal Component Analysis (PCA). So, it is important to become familiar with PCA and its applications. The PCA studies a data space (X matrix) in order to find the best descriptive axis by rotating its XYZ coordination system. The first principal component axis (PC1) passes through the mean center of the raw data and goes in a direction that maximizes the variance of the projections of each observation (Figure 28-left). The distance from the origin to the projection point of each observation is called the *score* of that observation. The collection of the N scores is a N×1 matrix and is called the score matrix (t_1), when there are K variables and N observations. The direction of PC1 is a K×1 vector that is called the loading vector (p_1).

To find the second principal components (PC2) one needs first to deflate the X matrix from what is already predicted by PC1.

$$X = \hat{X}_1 + E_1 = T_1 P'_1 + E_1 \qquad (12)$$

PC2 also passes through the origin (mean center) and is perpendicular to PC1 direction. Similarly, PC2 also acquires the direction that maximizes the variance the projection of the observations in E_1 onto it. PC2 has its own loading and score matrices (p_2 and t_2, respectively). For a PCA model with A principal components:

$$T_{N\times A} = X_{N\times K} P_{K\times A} \qquad (13)$$

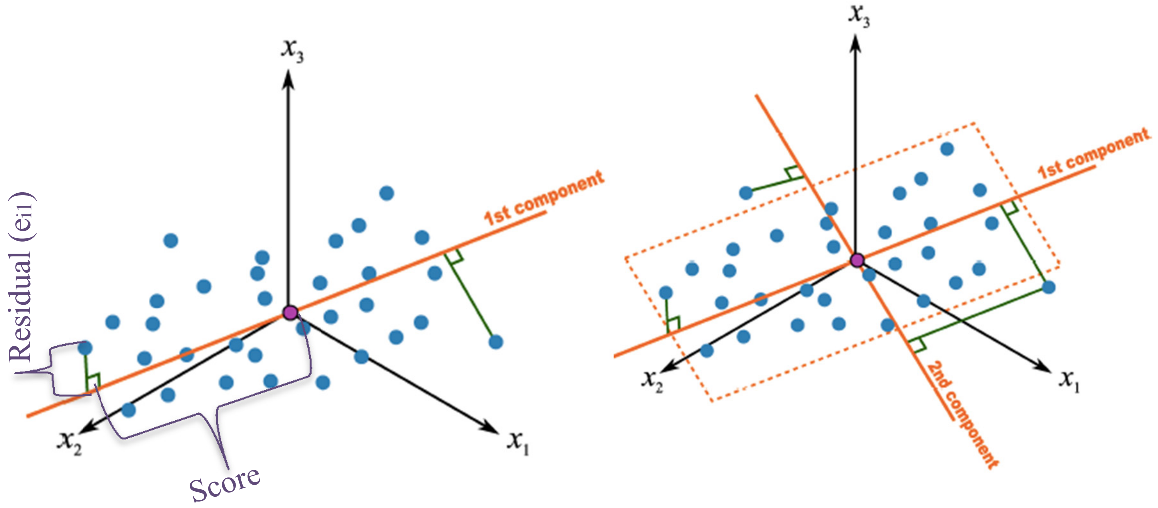

Figure 28- Finding the principal components in a cloud of data [117]

All the principal components together form a latent structure that describes the data. The perpendicular distance of each observation from the plane of principal components is the model residual error. So a PCA model explains a great part of the data and leaves some residuals.

$$X_{N\times K} = \hat{X}_{N\times K} + E_{N\times K} = T_{N\times A} P'_{A\times K} + E_{N\times K} \qquad (\ 14\ )$$

The sum of the residual for each observation i (each row of the E matrix) is called the *squared prediction error* (SPE). The SPE shows how each observation is consistent or inconsistent with the model (low or large SPE values, respectively). It can be used to detect the outlier data for each observation. For each column of E matrix the total error is called R^2_k. It explains the data from that column. The total modeling error is called R^2:

$$R^2 = 1 - \frac{Var(X-\hat{X})}{Var(X)} = 1 - \frac{Var(E)}{Var(X)} \quad (\ 15\ )$$

As one increases the number of components the R^2 value gets closer to the unity [117].

There are several methods to practically make a PCA model for an X matrix. The common method for PCA calculation is the Non-Linear Iterative Partial Least-Squares (NIPLAS), which extracts one principal component by repeating a series of calculation as described below:

1- Select a t_a score matrix with arbitrary values and regress every column of X matrix into t_a to get a 1×K p'_a loading matrix (Figure 29-a). Comparing with the ordinary regression solution for y=βx, in which $\beta = (X'X)^{-1}X'Y$:

$$p'_a = \frac{t'_a X}{t'_a t_a} \tag{16}$$

One should note that the loading vector must be of unit length. So $p'_a = \frac{1}{\sqrt{P'_a P_a}} P'_a$

2- Then one needs to regress each raw of the X matrix into p'_a to calculate new values for t_a (Figure 29-b). Similarly,

$$t_a = \frac{X p_a}{p'_a p_a} \tag{17}$$

3- One should repeat these two steps until the difference between last two t_a vectors becomes negligible (in the range of $1 \times 10^{-6}\ to\ 1 \times 10^{-9}$).

For the second component one needs to repeat step 1 to 3 over the residual of the first component. This action is called deflation.

$$X_a - t_a p'_a = E_a$$
$$X_{a+1} = E_a$$

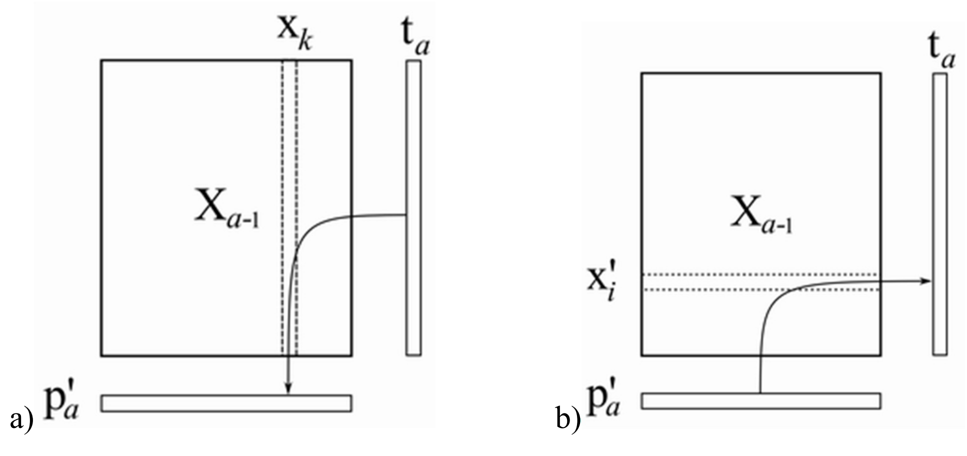

Figure 29- NIPLAS calculation for finding the PCAs

In order to determine the required number of PCs a "Cross-validation" method is used. It evaluates the effect of each new component using a parameter called Q^2. The Q^2 is the parameter that changes with addition of each new component. The new component is beneficial for the model, as long as the Q^2 value increases. However, after adding some components, Q^2 starts to decrease. This indicates that no more precision is added to the model by adding more PCs. A model is considered as a good explanation of the data space while $Q^2 \geq 0.5$ [105].

PLSR calculation

There are three simultaneous objectives in a PLSR model:

- Best explanation of the predictor matrix (X) structure ($t'_a t_a$)
- Best Explanation of the predicted matrix (Y) structure ($u'_a u_a$)
- The greatest relationship between X and Y which is given by the correlation between t_a and u_a.

Similar to the PCA method, the scores and the loadings should be extracted from X and Y matrices:

$$t_a = X_a w_a \qquad \text{For the X-space}$$

$$u_a = Y_a c_a \qquad \text{For the Y-space}$$

But with an additional limit; one should keep the maximum covariance between the scores (t_a and u_a).

$$Cov(t_a, u_a) = \mathrm{E}\{(t_a - \overline{t_a})(u_a - \overline{u_a})\} \qquad (18)$$

Similar to a PCA calculation (Figure 29) a series of iterative regression is needed to find the scores and the loadings for both X and Y matrices with some more constraints to realize PLSR objectives, as depicted in Figure 30. These four vectors t_a, u_a, w_a, and c_a determine the a^th principal component [117].

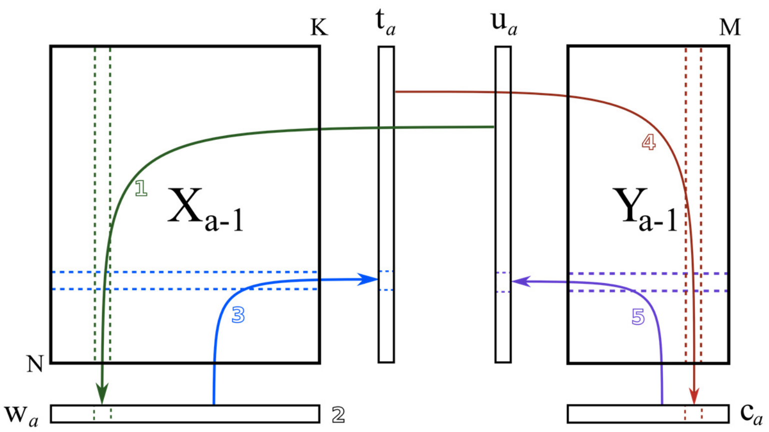

Figure 30- NIPLAS algorithm for determining components of PLSR model [117]

For the next component one needs to extract the explained part of the X and Y from the raw data.

$$E_a = X_a - \hat{X}_a = X_a - t_a w_a' \qquad (19)$$

$$X_{a+1} = E_a \qquad (20)$$

and

$$F_a = Y_a - \hat{Y}_a = Y_a - t_a c_a' \qquad (21)$$

$$Y_{a+1} = F_a \qquad (22)$$

Note that the t_a has been used for both X and Y deflations.

Similar to a PCA calculation, there are the R^2 value shows how well the model fits the data. Again as the number of components is increased, the R^2 value gets closer to unity. But the model does not necessarily get better. Svant Wold introduced a tool called the "cross validation" in order to determine the number of principal components [99]. It is based on evaluation of model prediction power, as a new PC is added. It divides the observations into G groups and select one of these groups, let call it group g. Therefor the X matrix is split into two parts of $X_{(g)}$ and $X_{(-g)}$. The cross validation tool builds a PCA model on $X_{(-g)}$ and then test it with $X_{(g)}$ that gets $\hat{X}_g$, and E_g. Repeating the same steps for all the G groups results in a matrix of errors ($E_{A.CV}$), in which A represents the number of principal components and CV indicates that this residual matrix is derived from cross-validation. A new parameter is then calculated from $E_{A.CV}$ in the same manner as R^2 value, which is called Q^2. There is also a Q^2_k that is calculated for each single principal component. This Q^2

is different from R^2. It is always smaller than R^2. In contrast with R^2 that always increases with number of A, it decreases after a certain number of principal components. As the Q^2 value begins to decrease it shows that the new components is not describing the structured part of X matrix anymore. As far as the Q^2_k value for a new component is greater than 0.0975, those components are considered as significant. A model is considered as a good explanation of the data space while the total $Q^2 \geq 0.5$ [105].

C. Electric probes

There are two main electric probes in plasma diagnostics:

- Faraday-cup
- Langmuir probe

Langmuir probe

Irving Langmuir demonstrated that the I-V characteristic curve of an isolated probe inserted into plasma medium provides reliable information about the electron density and electron temperature. This technique is then referred to as the Langmuir probe. Such a probe is basically an isolated electrode, usually a wire, connected to a power supply capable of biasing it at various positive and negative voltages relative to the plasma voltage. The type and the amount of the collected charges are proportional to the applied bias voltage. Electron Energy Distribution Function (EEDF), plasma density (N), and electron temperature (T_e) can be extracted through the interpretation of the resulted I-V curves [118,119]. Some specific conditions are required for such measurements like the distorted plasma size due to probe shape must be smaller than the electron mean free path.

Langmuir probe diagnostics is highly dependent on receiving the correct I-V curve and proper interpretation of the graph. Figure 31 shows a typical I-V curve. In this diagram plasma potential (space potential, V_s) is where exponential growth of I_e stops, that means all ions are repelled and the probe reaches to its electron saturation current. At far left side of the curve where the probe potential (V_p) is much more negative than plasma potential (V_s) (region I), an ion current is collected. At the left side of this region Ion saturation current can be measured. On the other side of the curve, where $V_p >> V_s$ (region III), lower energy electrons absorbed to the probe by increasing probe potential and an electron current is collected. The electron saturation current (I_{es}) could be an indication of electron density only at low plasma density and pressure where electrons mean free path is very long. It is better to measure plasma density by collecting ions.

In region II, V_p becomes negative with respect to V_s, so that a retarding field is setup for electrons and a positive field is developed for positive ions. In Maxwellian plasma, this part of the curve is exponential. The Floating Potential (V_f) is where the ion and electron currents are equal, and the net current is zero. It is clear that V_f is quiet different form V_s and probe potential at zero current cannot be considered as the plasma potential. V_s is located at the intersection of two lines passing through transition and electron saturation regions as illustrated in Figure 31.

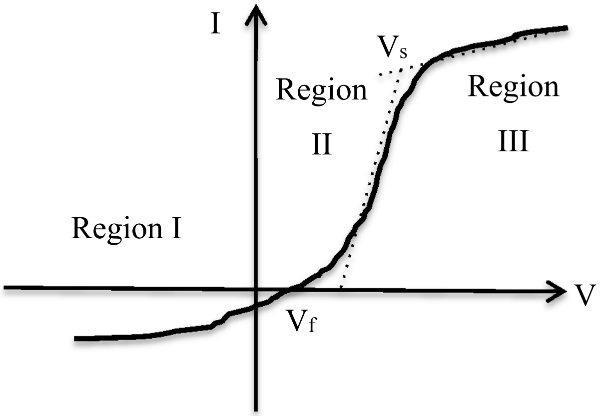

Figure 31: A typical I-V curve

If one applies a potential equal to plasma potential (V_p=V_s) then there is neither retarding nor accelerating potential for electrons and ions toward the probe. So probe current would be a function of the probability of electron or ions to be captured according to their energy level. Considering Maxwellian energy distribution then electron and ion current is [47,119]:

$$I_e = I_{es} = \frac{1}{4} A_p ne(8kT_e/\pi m)^{1/2} \quad (23)$$

And

$$I_i = \frac{1}{4} A_p ne(8kT_i/\pi M)^{1/2} \quad (24)$$

Where A_p is the probe surface area, n is the plasma density, e is the charge of electron or ion, T_e and T_i are the electron and the ion temperatures, and m and M are the mas of electron and ion, respectively. Knowing the fact that $T_e >> T_i$ and m<<M, the I_i would be negligible.

On the other hand at the V_p=V_f where the probe potential reach to floating potential, I_i and I_e become equal. Because in this region, probe potential is negative with respect to plasma potential and there is retarding potential against electron while there is an accelerating potential for ions. I_e is now like this:

$$I_e = \frac{1}{4} A_p ne(8kT_e/\pi m)^{1/2} \exp(-eV_\phi/kT_e) \qquad (25)$$

Where $V_\phi = V_s - V_p$. Comparing with Eq. $I_e = I_{es} = \frac{1}{4} A_p ne(8kT_e/\pi m)^{1/2}$ (23), we have

$$I_e = I_{es} \exp(-eV_\phi/kT_e) \quad (26)$$

It is clear that plotting Ln(I) against V_ϕ at the transition region of the I-V curve (region II) would result in a line, which its slope is exactly equal to e/KT$_e$ that is a good measure of electron temperature.

In region I, the probe is covered by a well-developed sheath and no electron reach the probe. Following equation gives the ion current (I$_i$) in this region: (when $\varepsilon_p = \frac{R_p}{\lambda_D} \gg 1$, where λ_D is Debye thickness and $\lambda_D = [\varepsilon_o T_e/eN_e]^{1/2}$)

$$I_i \approx 0.5\, A_p n_i e u_B \qquad (27)$$

in which u_B is Bohm velocity ($u_B = \sqrt{KT_e/M_i}$). Knowing T$_e$ and I$_i$ one can estimate plasma ion density (n$_i$).

In 1930s Druyvesteyn developed Langmuir's theory and showed that for a non-Maxwellian electron energy distribution, energy distribution function is related to the second derivative of probe current as a function of V_ϕ.

$$F(\epsilon) = \frac{4}{e^2 A_p} \sqrt{\frac{mV}{2e} \frac{d^2 I}{dV^2}} \qquad (28)$$

Figure 32 shows an experimental approach from I-V curve to the EEDF using Druyvesteyn methods.

Knowing energy distribution function ($F(\epsilon)$), either Maxwellian or Druyvesteyn, one can derive electron density and electron temperature according to Eqs. (29) and (30).

$$n_e = \int_0^\infty F(\epsilon)\, d\epsilon \qquad (29)$$

$$T_e = \frac{2}{3}\langle\epsilon\rangle = \frac{2}{3} n_e^{-1} \int_0^\infty \epsilon F(\epsilon)\, d\epsilon \qquad (30)$$

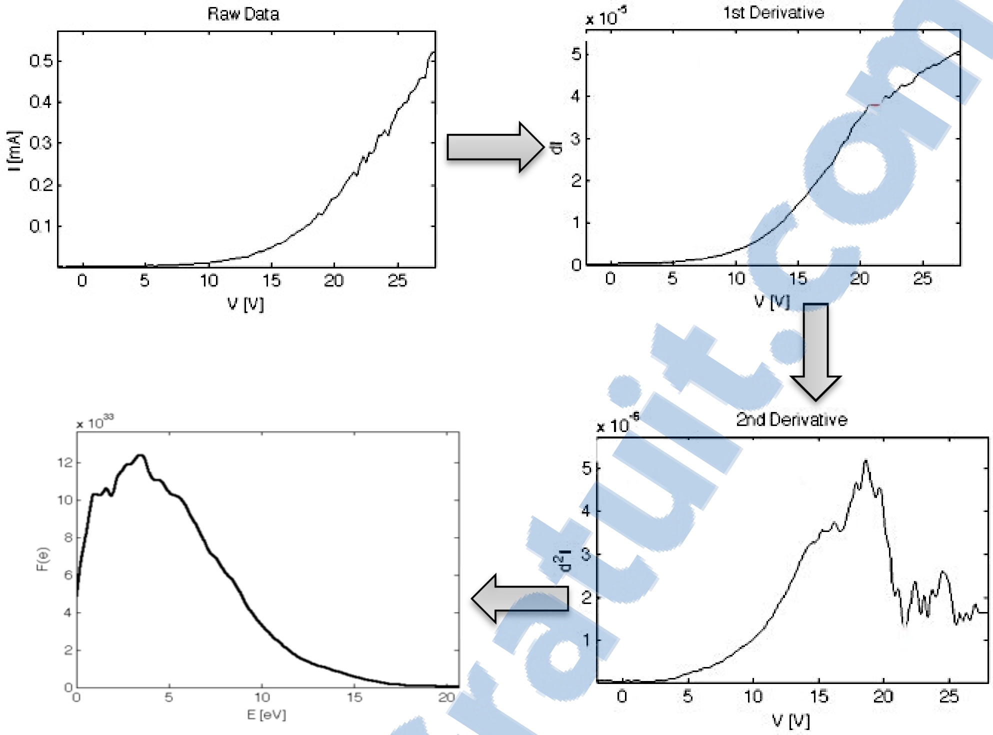

Figure 32: Application of Druyvesteyn method to achieve EEDF from I-V curve in an Langmuir probe experiment [120]

A number of considerations must be met to receive reliable results from Langmuir probe measurements[47,119]:

- Plasma perturbation or disturbance induced by probe should be kept as low as possible (use inert material).
- Probe dimensions should be much more than Debye sheath[1] thickness ($r_p \gg \lambda_D$). Otherwise, special consideration must be applied.
- Plasma pressure should be low in order to have a small sheath thickness compared to mean free path of charge carriers. A low pressure of 100 mTorr (or lower) is suitable for common probe measurements.
- Length of probe, which is exposed to plasma, should be long enough compared to its diameter, so that it could be considered as a cylindrical probe.

---

[1] Debye length is the distance in plasma over which significant deviation from neutrality, and therefore significant electrostatic fields, can exist.

- Effect of RF and probe circuit resistance on probe voltage need to be taken into consideration.
- Probe contamination is a problem that affects the measurements in reactive plasma. Rapid scanning and continuous probe cleaning (500-1500 $^{\circ}$C) through heating can mitigate this problem.

A simple design of a Langmuir probe was used in this study at the first step as a plasma diagnostic method. But as it just studies the electron related information, it was decided to replace it with another electric probe measurements, that is the Faraday-cup, which is capable of studying ions energy distribution.

Faraday-cup

The energy carried by plasma species is a key parameter in determining plasma surface interaction products. The ion energy distribution (IED) describes this energy. The Faraday-cup is a technique that is used to measure this parameter.

A Faraday-cup works based on Faraday's theory that explains how electric charges distribute on outer surface of a conductive material. The current of a charged object is a measure of the amount of charges that it receives at different biased voltage. This technique is used to understand the energy level of incident ions, which are bombarding the substrate surface. High-energy ions are adsorbed to the cup at lower voltage while low-energy ones need more voltage to be attracted.

This analyzer consists of a housing and an electrically isolated interior chamber, called Faraday cup (Figure 33). The housing is negatively charged to repel plasma free electrons. There is a small aperture on both housing and cup, which let the ions get into the cup. A range of voltage is applied to the cup to attract positive ions relative to their energy level.

Interpretation of the resulted I-V curve and its first derivative (dI/dV-V) provides information on ion energy level and ion energy distribution at plasma-surface interface.

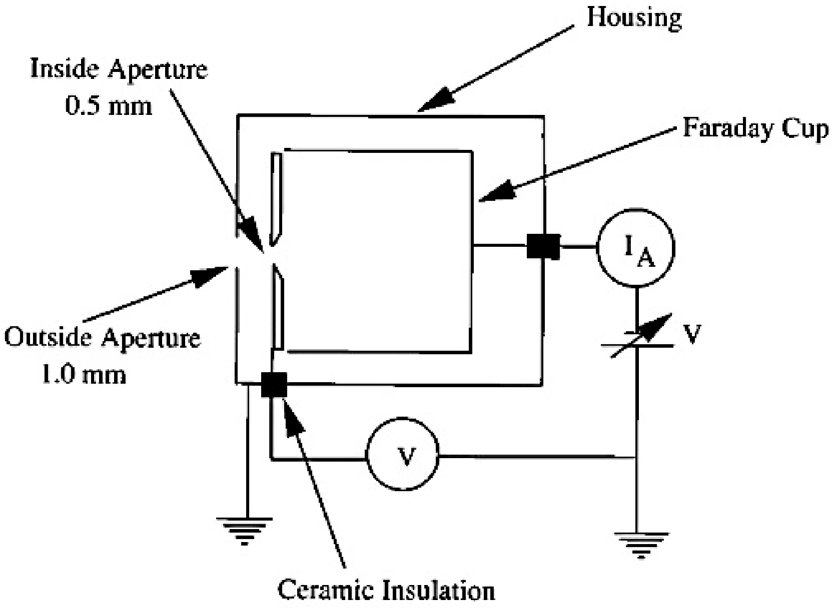

Figure 33: Schematic design of a Faraday cup [48].

When a charged object is placed inside the inner electrode, all the charge will flow into the measurement instrument. The electric field inside a closed, empty conductor is zero, so the cup shields the object placed inside it from any atmospheric or stray electric fields. This allows an accurate charge measurement. The I-V characteristic of the cup describes ion energy behavior inside plasma (Figure 34).

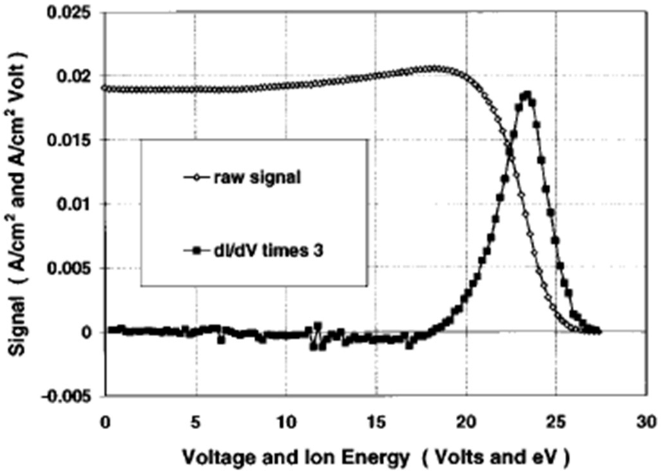

Figure 34- An example of I-V characteristic curve and its first derivative that explain ion energy distribution in plasma [35]

A homemade Faraday cup was designed and fabricated to study the plasma medium of the current work. Figure 35 shows different part of this probe. Also some sample graphs recorded at different plasma conditions are presented in Figure 36, 37 andFigure 38.

Plasma pressure effect on IED at different power in an Ar plasma medium is presented in Figure 36. The presence of second peak in energy distribution curve in evident in higher pressure.

What makes it difficult to employ this probe was the applied bias voltage. As may be seen in Figure 37, even at low level of bias voltage there would be a discharge that distorts the curve.

Figure 38 shows the plasma pressure effect at zero bias voltage and at different power levels in CH_4 plasma.

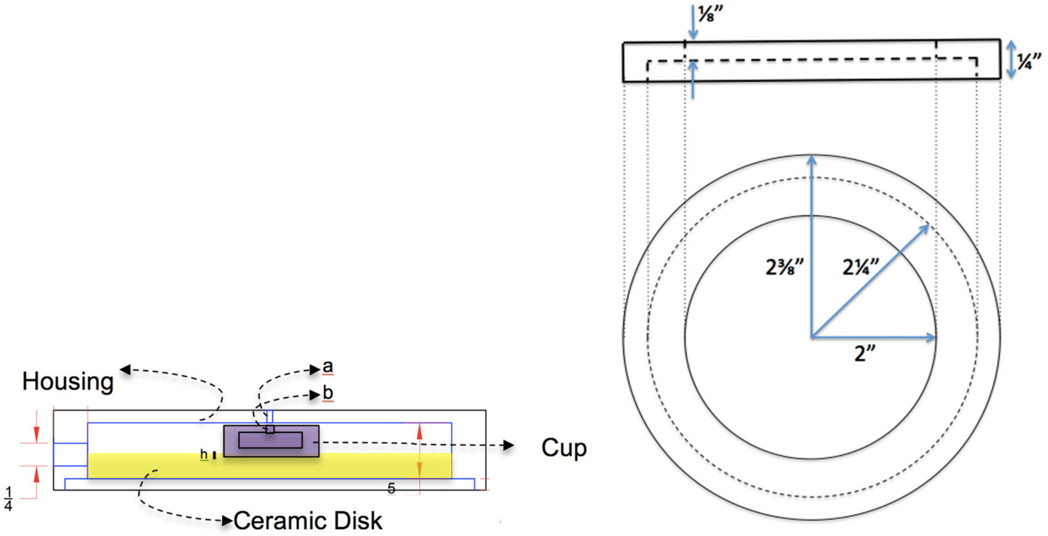

Figure 35- Different part of the Faraday's cup. a and b are the orifices on the housing and the cup for letting ions into the cup (right). The housing drawing, as it was fabricated to be used in the plasma reactor (left).

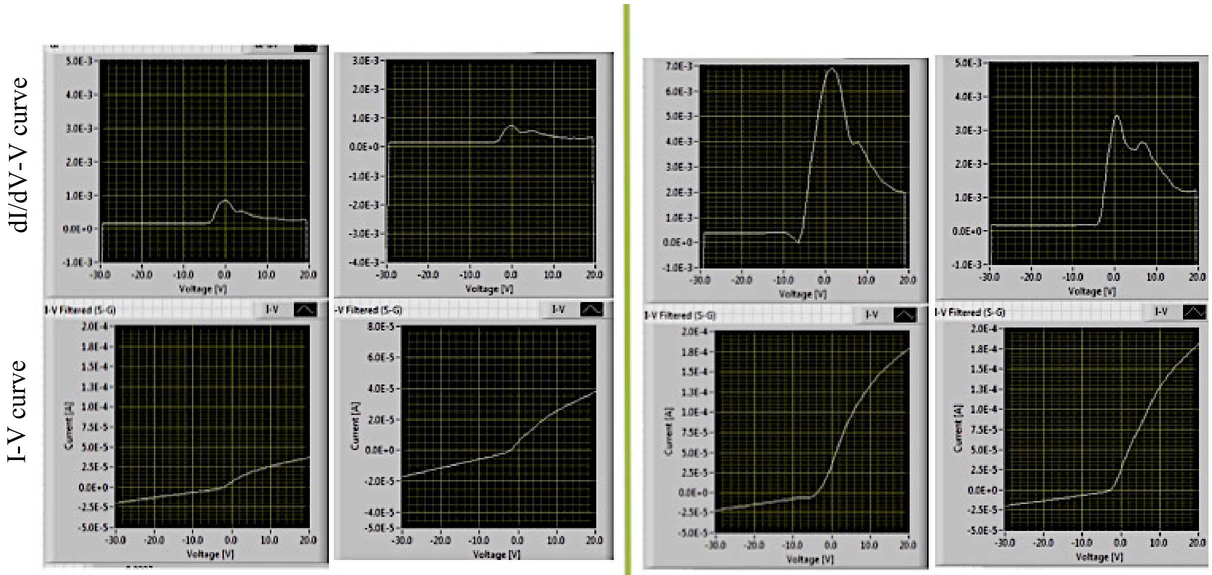

Pr: 17mTorr
Power: 100 W
Vb= 0 V

Pr: 50 mTorr
Power: 100 W
Vb= 0 V

Pr: 17mTorr
Power: 300 W
Vb= 0 V

Pr: 50 mTorr
Power: 300W
Vb= 0 V

Figure 36- Faraday's cup results at different Ar plasma condition.

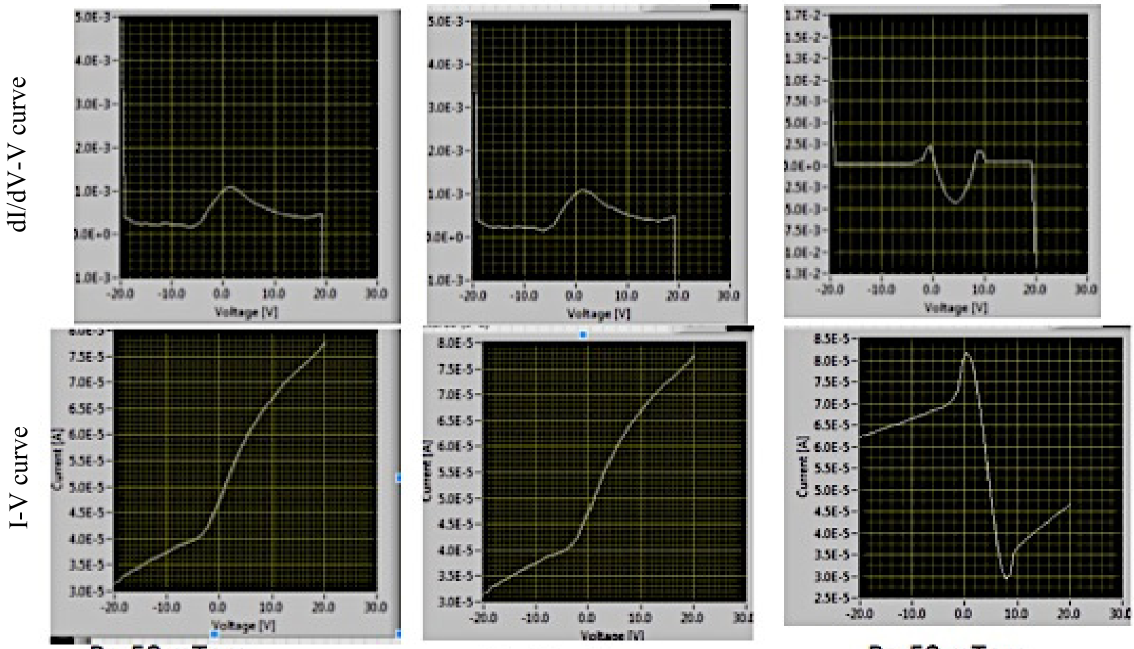

Pr: 50 mTorr
Power: 100 W
Vb= 0 V

Pr: 50 mTorr
Power: 100 W
Vb= -16 V

Pr: 50 mTorr
Power: 100 W
Vb= -28 V

Figure 37-Faraday's cup samples results for Ar plasma at different plasma conditions. I-V (top) and dI/dV-V graphs (bottom) are presented. The interrupted graph at medium bias voltage is marked in red.

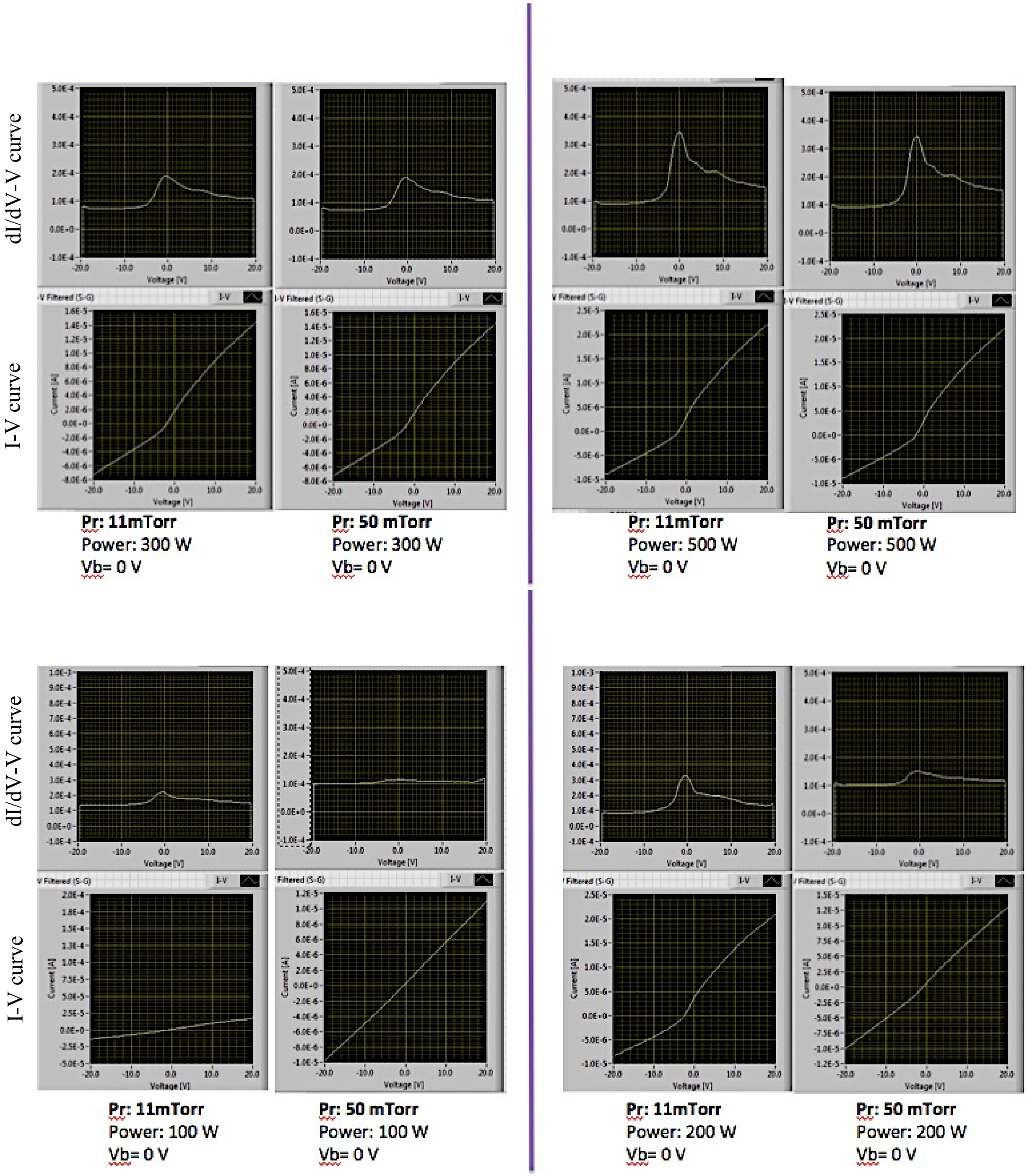

Pr: 11mTorr
Power: 300 W
Vb= 0 V

Pr: 50 mTorr
Power: 300 W
Vb= 0 V

Pr: 11mTorr
Power: 500 W
Vb= 0 V

Pr: 50 mTorr
Power: 500 W
Vb= 0 V

Pr: 11mTorr
Power: 100 W
Vb= 0 V

Pr: 50 mTorr
Power: 100 W
Vb= 0 V

Pr: 11mTorr
Power: 200 W
Vb= 0 V

Pr: 50 mTorr
Power: 200 W
Vb= 0 V

Figure 38- Faraday's cup samples results for CH_4 plasma at different plasma conditions. I-V graph (top) and dI/dV graphs (bottom) are presented for each plasma condition.